Physics of Fluids, Volume 35, Issue 10, October 2023, Article number 107137
DOI:10.1063/5.0169061

Accepted to Phys. Fluids 10.1063/5.0169061

Resonance mechanism of hydroelastic response of multi-patch floating photovoltaic structure in water waves over stepped seabed

Chongwei Zhang (张崇伟),[1,2] Pengfei Wang (王鹏飞),[2] Luofeng Huang (黄洛枫),[3] Mengke Zhang (张萌稞),[2] Haitao Wu (吴海涛),[4] and Dezhi Ning (宁德志)[2, a)]

[1)] *Marine Green Resources Research Center, Donghai Laboratory, Zhoushan 316021, People's Republic of China*

[2)] *State Key Laboratory of Coastal and Offshore Engineering, Dalian University of Technology, Dalian 116024, People's Republic of China*

[3)] *School of Water, Energy and Environment, Cranfield University, Cranfield MK43 0AL, UK*

[4)] *CIMC Gwind Co., Ltd., Block C, Shenzhen 518000, People's Republic of China*

(Dated: 7 September 2023)

Accepted to Phys. Fluids 10.1063/5.0169061

This paper investigates the hydroelastic response of a multi-patch floating photovoltaic (FPV) structure in water waves over a stepped seabed. The resonance conditions and underlying mathematical mechanism of FPV patches are explored based on linear potential-flow theory and the thin-plate model. An implicit function of the open-water wavelength and the FPV patch's structural wavelength is derived. Resonance conditions occur in the FPV patch when the patch length and structural wavelength (rather than the water wavelength, as commonly believed) satisfy certain proportions. Mathematical derivations are conducted to interpret the value of each proportion. Two resonance conditions are recognized based on the mathematical structure of the solution. The effects of a stepped seabed and adjacent patches on the resonance conditions and hydroelastic behavior of FPV structures are also investigated. For a given stiffness parameter, the resonance conditions of FPV patches are solely determined by the water depth. The distance between adjacent patches does not alter the resonance conditions of each patch. Resonance occurs in the water body between two patches when the ratio of patch distance to water wavelength takes certain proportional values. A resonant water body tends to amplify the oscillation amplitude of both patches. However, when two FPV patches and a constrained water body reach their theoretical resonance conditions at the same time, the oscillation amplitudes of both the seaward patch and the constrained free surface are evidently suppressed. The transmitted waves of an FPV structure are largely determined by the dynamics of the leeward patch.

[a)]Author to whom correspondence should be addressed: dzning@dlut.edu.cn.

Accepted to Phys. Fluids 10.1063/5.0169061

I. INTRODUCTION

Solar energy is a promising alternative to fossil fuels because of its wide distribution and sustainability. The most common application of solar energy is to directly convert light energy into electricity through photovoltaic (PV) systems.[1] Although on-land solar PV systems have been in operation for many years, the large site areas required, the need for optimal geographic locations, and the potential ecological impacts continue to constrain their development. In recent years, the development of floating photovoltaic (FPV) systems at offshore sites has emerged as a promising alternative for coastal regions.[2]

Taking into consideration the high costs of offshore construction and operations, large-scale FPV power stations are often planned to reduce the levelized cost of electricity. Large-scale FPV power stations are normally divided into multiple patches for ease of installation, maintenance, and further expansion. Each patch is composed of interconnected elements, and the whole system can be considered as an elastic blanket with uniform thickness and stiffness. As a practical example, a multi-patch FPV power station has been established in Yingshang County, in the east of Anhui Province, China, with a total capacity of 130 megawatts.[3]

From a hydrodynamic point of view, each FPV patch, which features a large span-to-depth ratio, behaves like a floating blanket on the water. Under the persistent excitation of ocean waves, such blanket-type floating structures inevitably experience hydroelastic vibrations, which is of the utmost importance for the fatigue design of the system. However, as a newly emerging field, the hydroelastic characteristics of various FPV systems have not yet been extensively studied.[4]

The few existing studies have mostly examined the dynamic responses of a single-patch FPV structure. For example, Choi and Lee[5] conducted finite element analysis and strength assessment for the frame structure of an FPV system under wind and wave loads. Dai *et al.*[6] considered an FPV system comprised of standardized floating modules made of high-density polyethylene. The structural performance of the floating modules and the inter-modular connectors were assessed through finite element analysis and laboratory tests. Al-Yacouby *et al.*[7] conducted a parametric study on the dynamic responses of a floating solar farm in regular waves using analytical and numerical methods. The effects of wave heights, wave periods, and pontoon diameters on the hydrodynamic forces and dynamic responses of the floating offshore solar farm were discussed. Xu *et al.*[8] analyzed the nonlinear fluid–structure interaction (FSI) of free-surface waves with a large-scale polymer FPV structure. A multi-time-scale perturbation method was used to solve the

nonlinear FSI model up to the second order. Zhang *et al.*[9] investigated the motion behavior of large arrays formed by multiple floaters hinged together, based on the potential flow theory and Rankine source panel method.

For multi-patch FPV structures, the effects of inter-patch connectors on the hydroelastic responses and internal loads of the structure are the primary point of interest. For example, Michailides *et al.*[10] conducted a numerical frequency-domain analysis of a modular floating structure with floating pontoons connected via flexible connectors in longitudinal and/or transverse directions. The effects of the connector's rotational stiffness and the pontoon layout on the hydroelastic responses of the structure and the connectors' internal loads were studied. Lee *et al.*[11] numerically analyzed the structural robustness of an FPV system under various wind and wave environments. Lee *et al.*[12] developed a numerical technique to predict the motion response of an FPV system in regular waves, with towing tank model tests conducted for validation.

As a vibration system with infinite degree-of-freedoms, a poorly designed FPV system may experience resonance oscillations under long-term excitation by ocean waves. The resonance mechanism, which determines the structural durability of an FPV system in water, has rarely been considered in previous studies, and should be carefully explored. Specifically, for a multi-patch FPV structure, three aspects of the resonance mechanism must be addressed:

- the resonance conditions of the FPV patches and their underlying mechanism;
- the effects of seabed topography on the resonance conditions of the FPV structure; and
- the effects of adjacent patches on the resonance conditions.

This study addresses the above three aspects from a mathematical point of view, aiming to provide a better understanding of the resonance mechanisms of multi-patch FPV structures in water waves.

Targeting the present hydroelastic problem, the methodology developed for the scenario of ice sheets can be used, even though the two scenarios have a different focus. Specifically, the ice scenario is mainly concerned with the water-wave field, whereas FPV systems have a greater dependence on the structural deformation properties.[13] As the thickness of ice sheets is negligible compared with their horizontal scale, elastic thin-plate theory is often introduced for ice-sheet analyses. Fox and Squire[14] considered the interaction between water waves and semi-infinite elastic plates, and analytically studied the wave transmission and reflection coefficients. Meylan and Squire[15] studied the interaction of waves with a finite-length elastic plate, and obtained an ap-

proximate solution for the reflection coefficient of waves. Andrianov and Hermans[16] obtained the amplitude distribution of elastic plate deflection under different incident wave angles, wavelengths, and water depths. Meylan and Sturova[17] analyzed the motion response of a two-dimensional finite-length elastic plate on the wave surface in the time domain. Maiti and Mandal[18] used symmetric and antisymmetric methods to study the interaction between waves and finite-length elastic plates. Singh *et al.*[19] studied the motion of a thin elastic plate that was either submerged in the water or floating on the free surface using Green's function.

An irregular seabed can have a noticeable effect on the characteristics of wave-structure interactions.[20] Wang and Meylan[21] used the boundary element method to analyze the linear wave force on a floating plate in water with variable depth. The reflection coefficient was found to be significantly different in water with variable and constant depths. Guo and Liu[22] analyzed the influence of a stepped bottom terrain on the wave scattering caused by a semi-infinite elastic plate.

For the multi-plate scenario, Porter and Evans[23] studied the scattering of flexural gravity waves propagating along an elastic ice sheet with multiple straight and parallel cracks in finite-depth water. Li *et al.*[24] further considered the propagation of flexural-gravity waves on a semi-infinite ice sheet with multiple cracks. Cracks with various shapes and locations were included. Marchenko[25] considered adjacent ice sheets based on the shallow-water hypothesis, and obtained the dispersion relationship of wave propagation in the ice-breaking channel. Ren *et al.*[26] focused on the water area between two semi-infinite elastic ice sheets, and discussed the motion of floating bodies in the water area between the ice sheets based on two-dimensional linear potential-flow theory. Shi *et al.*[27] analyzed the wave propagation through multiple ice-breaking channels based on the wide spacing approximation. Kostikov *et al.*[28] presented a nonlinear theoretical model for deformations, oscillations, and drift motions of multiple elastic ice sheets in shallow waters due to combined nonlinear waves and uniform current, based on the Green–Naghdi theory for the fluid motion and the thin plate theory for the deformation of the ice sheets.

This study focuses on an FPV structure consisting of two patches in ocean waves over a stepped seabed, as shown in Fig. 1. The aim is to obtain an in-depth explanation of the resonance conditions and underlying mathematical mechanism of the structure's hydroelastic responses. The FPV structure is analyzed using the thin-plate model. The mathematical model is established based on the eigenfunction matching method of linear potential-flow theory, which is described in Sec. II. The eigenfunction matching method, as one of the most well-established approaches for solving the Laplace equation,[29] has long become a classical analytical method for water wave

Accepted to Phys. Fluids 10.1063/5.0169061

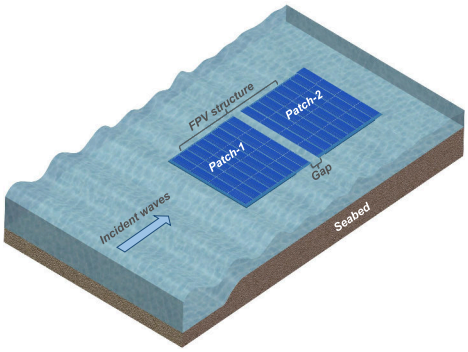

FIG. 1: Scenario of multi-patch FPV structure in ocean waves over stepped seabed.

problems.[30] The first piece of work on the interaction of water waves and a semi-infinite elastic plate may be traced back to Greehill.[31] In recent years, the method has been applied to investigate the hydroelastic interactions between water waves and submerged porous elastic disks of negligible thickness[32] and the scenario of wave-ice interactions.[33] In Sec. III, the mathematical mechanism behind the resonance conditions of the FPV structure is explored. The resonance behaviors of the FPV structure above a stepped seabed and the effects of adjacent or nearby patches on this resonance behavior are also investigated. Finally, the conclusions to this study are presented in Sec. IV.

II. MATHEMATICAL MODEL

A. Boundary value problem

The mathematical model of the multi-patch FPV structure in ocean waves over the stepped seabed is depicted in Fig. 2. The seaward patch is referred to as 'Patch-1' and the leeward patch is 'Patch-2'. The two patches have lengths of b_1 and b_2, respectively, and the distance between the two patches is D_s. Underneath the FPV structure there is a stepped seabed, which allows surface waves to propagate from deeper to shallower water. The water depth is represented by d, with $d = d_1$ and $d = d_0$ for the deeper and shallower regions, respectively.

Thin-plate theory is used to describe the dynamic behavior of each patch. The patches can be equivalently treated as floating plates. Both edges of each plate are free ends without constraints.

Accepted to Phys. Fluids 10.1063/5.0169061

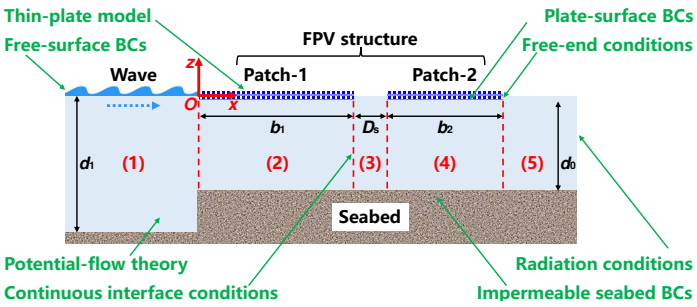

FIG. 2: Mathematical model of multi-patch FPV structure in ocean waves over stepped seabed.

A right-handed Cartesian coordinate system $O-xz$ is established, with the origin O on the still free surface at the left edge of Patch-1, the Oz-axis pointing upward, and the Ox-axis running along the direction of the incident waves. The hydroelastic problem of two floating plates in water waves is investigated based on potential-flow theory, whereby the fluid is assumed to be incompressible, inviscid, and irrotational. The velocity potential Φ, whose gradient is the fluid velocity, can be introduced. Both the structural response and wave motion are assumed to be steady with a small amplitude. The velocity potential can be expressed in the frequency domain as

$$\Phi(x,z,t) = \mathrm{Re}\left\{\phi(x,z)e^{-\mathrm{i}\omega t}\right\}, \tag{1}$$

where $\mathrm{i}^2 = -1$, ω is the angular frequency, ϕ is the spatial potential in complex field, and t is the time.

To acquire an analytical solution, the entire fluid domain is divided into five subdomains, i.e., V_1 with $(-\infty < x \le 0, -d_1 \le z \le 0)$, V_2 with $(0 \le x \le b_1, -d_0 \le z \le 0)$, V_3 with $(b_1 \le x \le a_1, -d_0 \le z \le 0)$, V_4 with $(a_1 \le x \le a_2, -d_0 \le z \le 0)$, and V_5 with $(a_2 \le x < \infty, -d_0 \le z \le 0)$. Here, $a_1 = b_1 + D_s$, $a_2 = a_1 + b_2$, and $b = b_1 + b_2 + D_s$. The superscript '(j)' is used to denote a variable in subdomain V_j.

In each subdomain V_j, the spatial potential satisfies the Laplace equation

$$\nabla^2 \phi^{(j)} = 0, \tag{2}$$

and the impermeable boundary condition (BC) on the seabed

$$\frac{\partial \phi^{(j)}}{\partial z} = 0 \text{ on } z = -d. \tag{3}$$

Both kinematic and dynamic BCs[34] are guaranteed on $z = 0$ as

$$\frac{\partial \phi^{(j)}}{\partial z} = -\mathrm{i}\omega\eta^{(j)} \tag{4}$$

and

$$\frac{p_{\mathrm{s}}^{(j)}}{\rho} = -\mathrm{i}\omega\phi^{(j)} - g\eta^{(j)} \tag{5}$$

where $\eta^{(j)}$ represents either the free-surface elevation or the vertical displacement of the plate element, ρ is the fluid density, g is the gravitational acceleration, and $p_{\mathrm{s}}^{(j)}$ refers to the hydrodynamic pressure on the fluid boundary.

On the free surfaces of V_1, V_3 and V_5, the zero-pressure assumption is made, with

$$p_{\mathrm{s}}^{(j)} = 0 \text{ with } j = 1, 3, \text{ or } 5. \tag{6}$$

Combining Eqs. (4), (5) and (6) leads to the free-surface BC in compact form

$$\frac{\partial \phi^{(j)}}{\partial z} = \frac{\omega^2}{g}\phi^{(j)} \text{ on } z = 0 \text{ with } j = 1, 3 \text{ or } 5. \tag{7}$$

On the lower surface of the plate, the dynamic pressure satisfies[34]

$$p_{\mathrm{s}}^{(j)} = EI\frac{\partial^4 \eta^{(j)}}{\partial x^4} + m_s\left(-\omega^2\eta^{(j)} + g\right) \text{ with } j = 2, \text{ or } 4, \tag{8}$$

where E is the Young's modulus of the elastic plate, $I = c^3/\left[12\left(1-\nu^2\right)\right]$, c is the plate thickness, ν is the Poisson's ratio, $m_s = \rho_s c$, and ρ_s is the plate density. Eliminating p_s and $\eta^{(j)}$ in Eqs. (4), (5) and (8) leads to a concise fluid boundary condition below the plate

$$\left(K\frac{\partial^4}{\partial x^4} + W\right)\frac{\partial \phi^{(j)}}{\partial z} - \phi^{(j)} = 0 \text{ on } z = 0 \text{ with } j = 2 \text{ or } 4, \tag{9}$$

with $K = EI/\rho\omega^2$, and $W = \left(\rho g - m_s\omega^2\right)/\rho\omega^2$. The free-end boundary conditions are satisfied on the left and right edge of each patch,[34] which allows

$$\frac{\partial^3 \phi^{(j)}}{\partial x^2 \partial z} = 0 \text{ and } \frac{\partial^4 \phi^{(j)}}{\partial x^3 \partial z} = 0 \text{ on } x = 0, b_1, a_1, \text{ or } a_2 \text{ and } z = 0 \text{ with } j = 2 \text{ or } 4. \tag{10}$$

The following radiation conditions are satisfied on the infinity boundary to complete the boundary value problem[34]

$$\frac{\partial \phi_{\mathrm{D}}}{\partial x} = \pm\mathrm{i}k\phi_{\mathrm{D}} \text{ on } x = \mp\infty, \tag{11}$$

$$\phi_{\mathrm{D}} = \phi - \phi_{\mathrm{I}}, \tag{12}$$

$$\phi_{\mathrm{I}} = -\frac{\mathrm{i}g}{\omega}\frac{H}{2}\frac{\cosh k(z+d)}{\cosh kd}e^{\mathrm{i}kx}, \tag{13}$$

where the subscripts D and I denotes the diffraction and incident components of the velocity potential, respectively. The radiation conditions allow the radiation and diffraction waves to propagate out of the fluid domain.

On each interface between adjacent subdomains, the pressure and normal velocity of the fluid should be continuous, which corresponds to the following relationships:

$$\phi^{(j)} = \phi^{(j+1)} \text{ on } x = 0, b_1, a_1, \text{ or } a_2 \text{ and } -d_0 \le z \le 0 \text{ with } j = 1, 2, 3, \text{ or } 4, \tag{14}$$

$$\frac{\partial \phi^{(1)}}{\partial x} = \begin{cases} 0, \text{ on } x = 0 \text{ and } -d_1 \le z \le -d_0, \\ \frac{\partial \phi^{(2)}}{\partial x} \text{ on } x = 0 \text{ and } -d_0 \le z \le 0 \end{cases}, \tag{15}$$

$$\frac{\partial \phi^{(j)}}{\partial x} = \frac{\partial \phi^{(j+1)}}{\partial x} \text{ on } x = b_1, a_1, \text{ or } a_2 \text{ and } -d_0 \le z \le 0 \text{ with } j = 2, 3, \text{ or } 4, \tag{16}$$

B. Eigenfunction expansion

The eigenfunction matching method is used to solve the boundary value problems of $\phi^{(j)}$. Based on the eigenfunction expansion method, the general solution of the spatial potential in each subdomain can be expressed as

$$\phi^{(1)}(x,z) = -\frac{igA}{\omega}\left[\begin{array}{l}(e^{ik_0^{(1)}x} + R_0 e^{-ik_0^{(1)}x})Z_0^{(1)}(z) \\ + \sum_{m=1}^{\infty} R_m e^{k_m^{(1)}x} Z_m^{(1)}(z)\end{array}\right], \tag{17}$$

$$\phi^{(2)}(x,z) = -\frac{igA}{\omega}\left[\begin{array}{l}(A_0 e^{i\lambda_0^{(2)}x} + B_0 e^{-i\lambda_0^{(2)}(x-b_1)})Y_0^{(2)}(z) \\ + \sum_{n=1}^{\infty} (A_n e^{-\lambda_n^{(2)}x} + B_n e^{\lambda_n^{(2)}(x-b_1)})Y_n^{(2)}(z)\end{array}\right], \tag{18}$$

$$\phi^{(3)}(x,z) = -\frac{igA}{\omega}\left[\begin{array}{l}C_0 e^{ik_0^{(3)}(x-b_1)} + D_0 e^{-ik_0^{(3)}(x-a_1)})Z_0^{(3)}(z) \\ + \sum_{m=1}^{\infty} (C_m e^{-k_m^{(3)}(x-b_1)} + D_m e^{k_m^{(3)}(x-a_1)})Z_m^{(3)}(z)\end{array}\right], \tag{19}$$

$$\phi^{(4)}(x,z) = -\frac{igA}{\omega}\left[\begin{array}{l}(E_0 e^{i\lambda_0^{(4)}(x-a_1)} + F_0 e^{-i\lambda_0^{(4)}(x-a_2)})Y_0^{(4)}(z) \\ + \sum_{n=1}^{\infty} (E_n e^{-\lambda_n^{(4)}(x-a_1)} + F_n e^{\lambda_n^{(4)}(x-a_2)})Y_n^{(4)}(z)\end{array}\right], \tag{20}$$

$$\phi^{(5)}(x,z) = -\frac{igA}{\omega}\left[\begin{array}{l}T_0 e^{ik_0^{(5)}(x-a_2)}Z_0^{(5)}(z) \\ + \sum_{m=1}^{\infty} T_m e^{-k_m^{(5)}(x-a_2)}Z_m^{(5)}(z)\end{array}\right], \tag{21}$$

where A is the amplitude of the incident waves and A_n, B_n, C_m, D_m, E_n, F_n, R_m, and T_m are unknown coefficients. As elaborately explained in Appendix A, the terms $k_0^{(j)}$ and $k_m^{(j)}$ are positive real roots

of the following dispersion equations:

$$\omega^2 = gk_0^{(j)} \tanh k_0^{(j)} d^{(j)}, \tag{22}$$

$$\omega^2 = -gk_m^{(j)} \tan k_m^{(j)} d^{(j)} \tag{23}$$

for j =1, 3, or 5, and $\lambda_0^{(j)}$ and $\lambda_n^{(j)}$ are solutions of the following equations:

$$\lambda_0^{(j)} \left(K(\lambda_0^{(j)})^4 + W \right) \tanh \lambda_0^{(j)} d_0 = 1, \tag{24}$$

$$-\lambda_n^{(j)} \left(K(\lambda_n^{(j)})^4 + W \right) \tan \lambda_n^{(j)} d_0 = 1 \tag{25}$$

for j = 2 or 4. Note that $\lambda_0^{(j)}$, $\lambda_3^{(j)}$, $\lambda_4^{(j)}$, $\cdots$ are real, while $\lambda_1^{(j)}$ and $\lambda_2^{(j)}$ are a pair of complex conjugates. The values of $k_0^{(j)}$, $k_m^{(j)}$, $\lambda_0^{(j)}$, and $\lambda_n^{(j)}$ can be determined through an iterative procedure based on the image of the implicit function; details are given in Appendix B.

The terms $Z_0(z)$, $Z_m(z)$, $Y_0(z)$, and $Y_n(z)$ are vertical eigenfunctions of the form

$$Z_m^{(j)}(z) = \begin{cases} \cosh k_0^{(j)} \left(z + d^{(j)} \right) / \cosh k_0^{(j)} d^{(j)} \text{ for } m = 0 \\ \cos k_m^{(j)} \left(z + d^{(j)} \right) / \cos k_m^{(j)} d^{(j)} \text{ for } m \geq 1 \end{cases}, \; j = 1, 3, \text{ or } 5, \tag{26}$$

$$Y_n^{(j)}(z) = \begin{cases} \cosh \lambda_0^{(j)} (z + d_0) / \cosh \lambda_0^{(j)} d_0 \text{ for } n = 0 \\ \cos \lambda_n^{(j)} (z + d_0) / \cos \lambda_n^{(j)} d_0 \text{ for } n \geq 1 \end{cases}, \; j = 2 \text{ or } 4. \tag{27}$$

For convenience of expression, the inner product operator $< *, * >_b^a$ is introduced as

$$< f(z), g(z) >_b^a = \int_b^a f(z) g(z) dz. \tag{28}$$

The vertical eigenfunctions in V_1, V_3, and V_5 satisfy the orthogonal relationship

$$< Z_m^{(1)}, Z_n^{(1)} >_{-d_1}^0 = < Z_m^{(3)}, Z_n^{(3)} >_{-d_0}^0 = < Z_m^{(5)}, Z_n^{(5)} >_{-d_0}^0 = 0 \text{ for } m \neq n, \tag{29}$$

while for those in V_2 and V_4,

$$< Y_m^{(j)}, Y_n^{(j)} >_{-d_0}^0 = -K \left\{ \frac{\partial Y_m^{(j)}}{\partial z} \frac{\partial^3 Y_n^{(j)}}{\partial z^3} + \frac{\partial^3 Y_m^{(j)}}{\partial z^3} \frac{\partial Y_n^{(j)}}{\partial z} \right\}_{z=0} \neq 0 \text{ for } m \neq n \text{ with } j = 2 \text{ or } 4. \tag{30}$$

A new inner product operator $<< *, * >>_b^a$ is introduced:

$$\begin{aligned} << Y_m^{(j)}, Y_n^{(j)} >>_{-d_0}^0 &= < Y_m^{(j)}, Y_n^{(j)} >_{-d_0}^0 \\ &+ K \left\{ \frac{\partial Y_m^{(j)}}{\partial z} \frac{\partial^3 Y_n^{(j)}}{\partial z^3} + \frac{\partial^3 Y_m^{(j)}}{\partial z^3} \frac{\partial Y_n^{(j)}}{\partial z} \right\}_{z=0} \text{ with } j = 2 \text{ or } 4, \end{aligned} \tag{31}$$

which establishes the following orthogonal relationship:[34]

$$<< Y_m^{(j)}, Y_n^{(j)} >>_{-d_0}^{0} = 0 \text{ for } m \neq n \text{ with } j = 2 \text{ or } 4, \tag{32}$$

$$<< Y_n^{(j)}, Y_n^{(j)} >>_{-d_0}^{0} = \begin{cases} \dfrac{2\lambda_0^{(j)} d_0 + \sinh 2\lambda_0^{(j)} d_0 + 8K\left(\lambda_0^{(j)}\right)^5 \sinh^2 \lambda_0^{(j)} d_0}{4\lambda_0^{(j)} \cosh^2 \lambda_0^{(j)} d_0} & \text{for } n = 0 \\ \dfrac{2\lambda_n^{(j)} d_0 + \sin 2\lambda_n^{(j)} d_0 - 8K\left(\lambda_n^{(j)}\right)^5 \sin^2 \lambda_n^{(j)} d_0}{4\lambda_n^{(j)} \cos^2 \lambda_n^{(j)} d_0} & \text{for } n \geq 1 \end{cases} \quad \text{with } j = 2 \text{ or } 4. \tag{33}$$

The orthogonal relationship among the vertical eigenfunctions can be used to simplify the matching conditions on each interface, the details of which are given in Appendix C.

C. Calculation of physical quantities

A linear system of equations can be established by truncating the series expansions of $\phi^{(j)}$ after M terms and applying the matching conditions on the interfaces at $x = 0$, b_1, a_1, and a_2. The unknowns A_n, B_n, C_m, D_m, E_n, F_n, R_m, and T_m are determined following the process in Appendix D. Then, the explicit expressions for $\phi^{(j)}$ in each subdomain can be obtained.

The free-surface elevation in V_1, V_3, and V_5 and the vertical displacement of the plate in V_2 and V_4 can be calculated as

$$\eta^{(j)}(x,t) = \mathrm{Re}\left(\frac{\mathrm{i}}{\omega} \frac{\partial \phi^{(j)}}{\partial z} e^{-\mathrm{i}\omega t} \right) \text{ on } z = 0 \text{ with } j = 1,2,3,4, \text{ and } 5. \tag{34}$$

The incident and reflected wave components can be distinguished from Eq. (17), with

$$\phi_0(x,z) = -\frac{\mathrm{i}gA}{\omega} e^{\mathrm{i}k_0^{(1)} x} Z_0^{(1)}(z), \tag{35}$$

$$\phi_r(x,z) = -\frac{\mathrm{i}gA}{\omega} R_0 e^{-\mathrm{i}k_0^{(1)} x} Z_0^{(1)}(z). \tag{36}$$

The amplitudes of the incident and reflected waves, i.e., $\eta_0(x,t)$ and $\eta_r(x,t)$, can be obtained using Eq. (34). The reflection coefficient R and transmission coefficient T are expressed as

$$R = |\eta_r| / |\eta_0| = |R_0|, \tag{37}$$

$$T = \left|\eta^{(5)}\right| / |\eta_0| = |T_0|. \tag{38}$$

Accepted to Phys. Fluids 10.1063/5.0169061

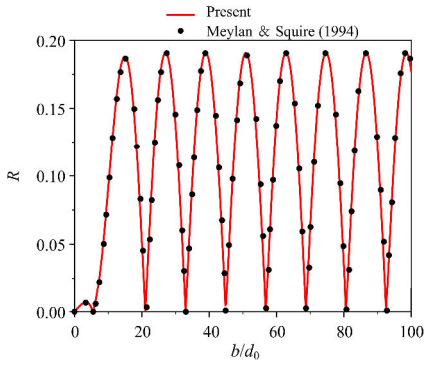

FIG. 3: Wave reflection coefficients of single elastic plate with different lengths in waves of L_w = 100 m. The wave reflection coefficients obtained from the present method agree well with those in the reference.

III. RESULTS AND DISCUSSION

A. Verification of mathematical model

The results of Meylan and Squire[35] are first reproduced to verify the present mathematical model. Unlike the eigenfunction expansion method in the present study, Meylan and Squire[35] used a Green's function method. A single finite-length elastic plate floating on the free surface with uniform water depth is considered. Free-end conditions are satisfied at both edges of the plate. The parameters are set as ρ_s = 922.5 kg/m^3, $E = 6 \times 10^9$ Pa, I = 0.086 m^3, μ = 0.3, c = 1 m, $d_1 = d_0$ = 5 m, and $D_s = b_2$ = 0. Unless specifically stated, the environmental parameters are ρ = 1025 kg/m^3, g = 9.81 m/s^2, and d_0 = 10 m in this study. The wavelength of the incident waves is $L_w = 2\pi/k_0 = 10d_0$. Figure 3 shows the wave reflection coefficient R of the plate. For plates of different lengths, the wave reflection coefficients obtained from the present method agree well with those of Meylan and Squire,[35] which verifies the reliability of the present numerical method.

B. Resonance conditions of FPV patch

This subsection explores the mathematics relating to the resonance conditions of the FPV patch. Hereafter, the physical parameters of the FPV patches are set as ρ_s = 950 kg/m^3, $c = 0.01d_0$,

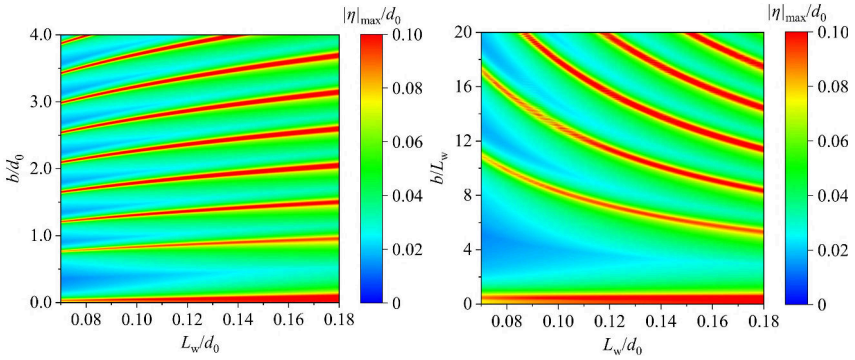

(a) (b)

FIG. 4: Distribution of maximum oscillation amplitude of FPV patch versus dimensionless wavelength and dimensionless plate length, with b nondimensionalized by (a) d_0 and (b) L_{w}. To maintain the resonance of the FPV patch, the plate length b must grow with the wavelength L_{w}, but with a decrease in the ratio of b/L_{w}.

$EI/\rho g d_0^4 = 0.005$, and $\nu = 0.38$. For an isolated FPV patch with different plate lengths b, the maximum oscillation amplitude measured on the patch (i.e., $|\eta|_{\mathrm{max}}$) for different incident wavelengths L_w is shown in Fig. 4. In Figs. 4(a) and 4(b), the plate lengths are nondimensionalized by d_0 and L_{w}, respectively. With a specific b, the resonance conditions for the FPV patch can be identified as the values of $|\eta|_{\mathrm{max}}$ that attain a local maxima as the wavelength increases. From Fig. 4(a), to maintain the resonance of the FPV patch, the plate length must grow with the wavelength, but with a decrease in b/L_{w}, as shown by Fig. 4(b). From an alternative perspective, in waves with a specific wavelength, a sequence of plate lengths can lead to resonant vibrations in the FPV patch. However, the relationship between the plate length b and water wavelength L_{w}, which reflects the mechanism behind the resonance conditions, is unclear from Fig. 4.

From a physical point of view, water bodies with a free surface and an elastic floating plate can be considered as two distinct media for propagating waves. As regular waves propagate from open water to the elastic plate, the wave frequency ω is invariable, but the wavelength changes from L_{w} to L_{b}. Hereafter, L_{b} can be referred to as the structural wavelength, satisfying $L_{\mathrm{b}} = 2\pi/\lambda_0$. The

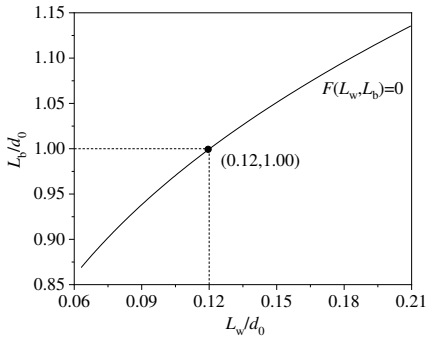

FIG. 5: Implicit function $F(L_w, L_b)$ as a one-to-one mapping of L_b and L_w. The structural wavelength L_b and the water wavelength L_w satisfy a nonlinear one-to-one mapping relationship.

dispersion equations (22) and (24) can be rewritten in terms of L_w and L_b as

$$\frac{\omega^2}{g} = \left(\frac{2\pi}{L_w}\right)\tanh\left(\frac{2\pi}{L_w}\right)d_0, \tag{39}$$

$$\left(\frac{2\pi}{L_b}\right)\left[K\left(\frac{2\pi}{L_b}\right)^4 + W\right]\tanh\left(\frac{2\pi}{L_b}\right)d_0 = 1. \tag{40}$$

Thus, the implicit function $F(L_w, L_b)$ can be generated as

$$F(L_w, L_b) = F_w(L_w) - F_b(L_b) = 0, \tag{41}$$

$$F_w(L_w) = \frac{L_w}{\tanh\frac{2\pi}{L_w}d_0}, \tag{42}$$

$$F_b(L_b) = \frac{L_b^4\left(\rho L_b + 2\pi m_s \tanh\frac{2\pi}{L_b}d_0\right)}{\rho\tanh\frac{2\pi}{L_b}d_0\left(L_b^4 + 16\pi^4 V d_0^4\right)}. \tag{43}$$

Figure 5 plots the implicit function $F(L_w, L_b)$ for the same case as Fig. 4, indicating that structural wavelength L_b and the water wavelength L_w satisfy a one-to-one mapping relationship.

With the known relationships of L_w and L_b, the distribution of the maximum oscillation amplitude of the FPV patch in Fig. 4 is replotted in Fig. 6, with b nondimensionalized by L_b. This makes it much easier to identify the resonance conditions. The resonance conditions for the FPV patch occur when the plate length and structural wavelength satisfy some proportional relationships, i.e., $b/L_b = \zeta$. For the present case, the first six proportions of ζ are $\zeta_1 \approx 0.86$, $\zeta_2 \approx 1.36$, $\zeta_3 \approx 1.86$, $\zeta_4 \approx 2.36$, $\zeta_5 \approx 2.86$, and $\zeta_6 \approx 3.36$. The interval between neighboring values of ζ is approximately

Accepted to Phys. Fluids 10.1063/5.0169061

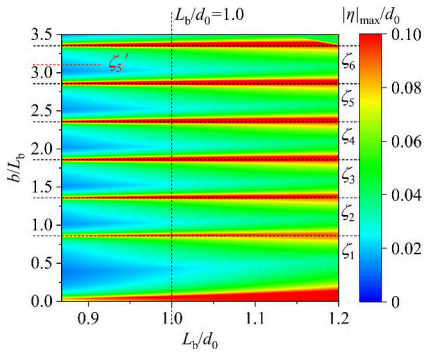

FIG. 6: Distribution of maximum oscillation amplitude of FPV patch versus dimensionless wavelength and dimensionless plate length, with b nondimensionalized by L_b. The resonance conditions for the FPV patch occur when the plate length and structural wavelength satisfy some proportional relationships.

0.50. Thus, once the first value of $\zeta = \zeta_1$ is identified, the remaining resonance conditions of the FPV patch can be found without difficulty.

Note that structural wavelength L_b is determined by the water depth below the FPV patch and the stiffness properties of the plate, but is independent of the plate length b. The stiffness properties of the plate can be expressed by the dimensionless parameter $V = EI/\rho g d_0^4$. In the present study, the stiffness parameter is set as $V = 0.005$. As V varies between 0 and 0.009, the implicit functions $F(L_w, L_b)$ are as shown in Fig. 7. In the same wave condition, the structural wavelength L_b increases with the stiffness parameter V. In the limiting condition with zero stiffness (i.e. $V = 0$), the plate behaves as if it does not exist, and the structural and water wavelengths coincide (i.e. $L_b = L_w$).

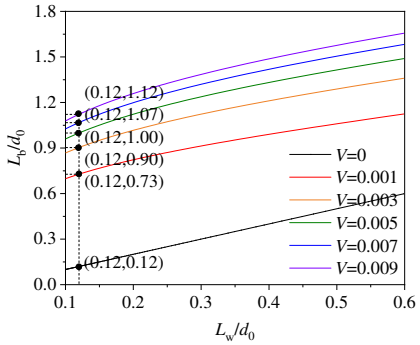

FIG. 7: Implicit function $F(L_w, L_b)$ with stiffness parameter V varying between 0 and 0.009. Under the same water wavelength L_w, the structural wavelength L_b increases with the stiffness parameter V.

C. Mathematics behind hydroelastic resonance of FPV patches

Mathematical derivations are now carried out to identify the value of ζ_1. The vertical displacement of an FPV patch in the steady state can be expressed as

$$\eta^{(2)}(x,t) = \tilde{A}\mathrm{Re}\left[\tilde{\eta}(x)e^{-\mathrm{i}\omega t}\right], \tag{44}$$

$$\tilde{A} = \left(gA\lambda_0^{(2)}/\omega^2\right)\tanh\lambda_0^{(2)}d_0, \tag{45}$$

$$\tilde{\eta}(x) = A_0 e^{\mathrm{i}\lambda_0^{(2)}x} + B_0 e^{\mathrm{i}\lambda_0^{(2)}b} e^{-\mathrm{i}\lambda_0^{(2)}x}. \tag{46}$$

In a specific wave condition, the coefficient $\tilde{A}$ is a real constant, which does not affect the resonance condition. The maximum oscillation amplitude of the FPV patch is solely determined by the maximum modulus of the complex quantity $|\tilde{\eta}(x)|$. The coefficients A_0 and B_0 can be written in complex form as $A_0 = A_\mathrm{r} + A_\mathrm{i}\mathrm{i}$ and $B_0 = B_\mathrm{r} + B_\mathrm{i}\mathrm{i}$. Here, A_r and B_r are the real parts, and A_i and B_i are the imaginary parts. Thus, Eq. (46) can be expressed as

$$|\tilde{\eta}(x)| = \alpha_1 + \alpha_2\cos\left(\lambda_0^{(2)}b - 2\lambda_0^{(2)}x\right) + \alpha_3\sin\left(\lambda_0^{(2)}b - 2\lambda_0^{(2)}x\right) \tag{47}$$

with

$$\alpha_1 = |A_0|^2 + |B_0|^2, \tag{48}$$

$$\alpha_2 = 2\left(A_\mathrm{i}B_\mathrm{i} + A_\mathrm{r}B_\mathrm{r}\right), \tag{49}$$

$$\alpha_3 = 2\left(A_\mathrm{i}B_\mathrm{r} - A_\mathrm{r}B_\mathrm{i}\right). \tag{50}$$

Accepted to Phys. Fluids 10.1063/5.0169061

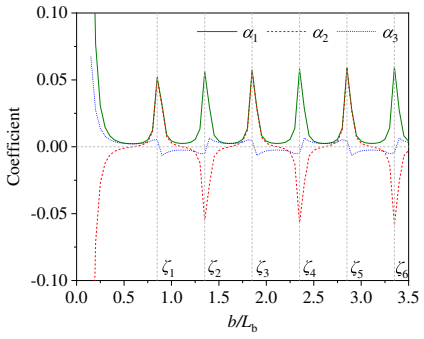

FIG. 8: Coefficients α_1, α_2, and α_3 versus b/L_b for $L_b/d_0 = 1.0$. The values of ζ_i are the ratios of b/L_b that produce local maxima of α_1.

The wave condition of $L_b/d_0 = 1.0$ (as indicated in Fig. 6) is taken as an example. Figure 8 shows the variation of α_1, α_2, and α_3 versus the ratio b/L_b. This study mainly focuses on the long-plate situation with $b/L_b > 0.5$. As b/L_b increases from 0.5 to 3.5, α_1 reaches a positive maximum at every ζ_i. In contrast, α_2 reaches a positive maximum at $b/L_b = \zeta_1$, ζ_3, and ζ_5, but a negative maximum at $b/L_b = \zeta_2$, ζ_4, and ζ_6. The magnitude of α_3 is much smaller than that of α_1 and α_2, and so it has less effect on the maximum modulus of $\tilde{\eta}$. Thus, the values of ζ_i are the ratios of b/L_b that produce local maxima of α_1, while $\alpha_1 = |A_0|^2 + |B_0|^2$ is determined by the amplitude of two bidirectional propagating wave components along the FPV patch.

Referring to Eq. (47), the maximal value of $|\tilde{\eta}|$ occurs when the following two conditions are satisfied:

- Odd condition: $b/L_b = \zeta_i$ with $i = 1, 3, 5, \cdots$ and $\cos\left(\lambda_0^{(2)} b - 2\lambda_0^{(2)} x\right) = 1$;
- Even condition: $b/L_b = \zeta_i$ with $i = 2, 4, 6, \cdots$ and $\cos\left(\lambda_0^{(2)} b - 2\lambda_0^{(2)} x\right) = -1$.

The odd and even conditions require $\lambda_0^{(2)} b - 2\lambda_0^{(2)} x = \pm 2n\pi$ and $\lambda_0^{(2)} b - 2\lambda_0^{(2)} x = \pi \pm 2n\pi$, respectively, with $n \in \{0, 1, 2\cdots\}$. The relations $\lambda_0^{(2)} = 2\pi/L_b$ and $b/L_b = \zeta_i$ are also satisfied. Under the constraint that $x \in [0, b]$, this yields

$$x/b = 1/2 \pm n/2\zeta_i \text{ with } 0 \le n \le \zeta_i \text{ for the odd condition,} \tag{51}$$

$$x/b = 1/2 - (1 \pm 2n)/4\zeta_i \text{ with } (-1 - 2\zeta_i)/2 \le \pm n \le (-1 + 2\zeta_i)/2 \text{ for the even condition.} \tag{52}$$

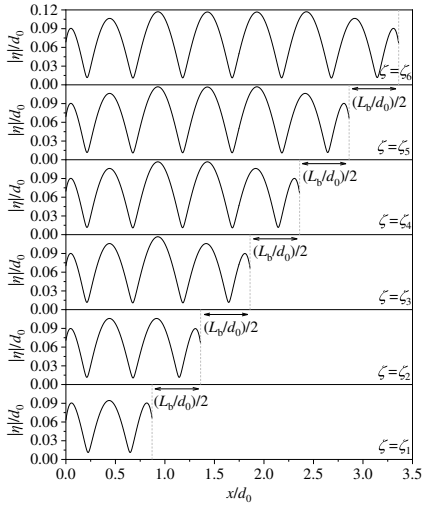

FIG. 9: Distribution of vertical oscillation amplitude of elements along FPV patch at resonance for L_b/d_0=1.0. When resonance occurs, the distribution of the oscillation amplitude on the FPV patch is symmetrical about the middle point of the plate.

Thus, all possible locations of the largest oscillation amplitude on the FPV patch are identified.

Figure 9 considers the example of an incident wave condition with $L_b/d_0 = 1.0$, and shows the distribution of the vertical oscillation amplitude along the FPV patch at resonance conditions of $b/L_b = \zeta_1$ to ζ_6. For case ζ_i, there exist $i+2$ peaks in the oscillation amplitude distribution along the FPV patch, which is consistent with the predictions in Eqs. (51) and (52). In the odd condition, the maximum oscillation amplitude appears in the middle of the plate, i.e., at $x = b/2$. In the even condition, the locations of the maximum oscillation amplitude are around the middle of the plate. In other words, when resonance occurs, the distribution of the oscillation amplitude on the FPV patch is symmetrical about the middle point of the plate. For each specific wave condition, as the plate length increases, the plate experiences a series of resonance conditions. The difference in plate length between adjacent resonance conditions is around $L_b/2d_0$, the periodicity of which can be confirmed by substituting Eq. (18) into the free-end boundary conditions.

Figure 10 shows the distribution of the wave transmission coefficient versus the dimensionless wavelength and dimensionless plate length, with b nondimensionalized by L_b. Comparing Figs. 6 and 10, it is clear that the oscillation resonance of the FPV patch produces a maximum wave

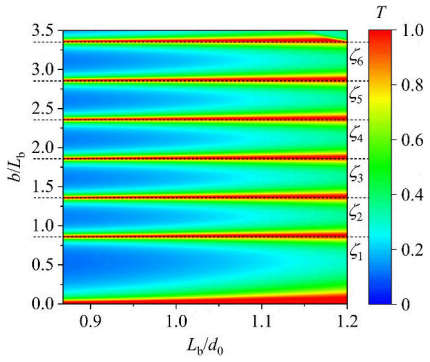

FIG. 10: Distribution of wave transmission coefficient versus dimensionless wavelength and dimensionless plate length, with b nondimensionalized by L_{b}. Comparing Figs. 6 and 10, the oscillation resonance of the FPV patch produces a maximum wave transmission coefficient.

transmission coefficient. Under resonance, the oscillating plate works as a wave generator, which increases the wave transmission coefficient.

D. Resonance behavior of FPV patch above stepped seabed

Underwater topography is another factor affecting the resonance conditions and hydroelastic behavior of an FPV patch. This subsection investigates the effects of a stepped seabed. The stepped seabed allows surface waves to propagate from deeper water (with $d = d_1$) to shallower water (with $d = d_0$). The FPV patch is located at the edge of the stepped seabed, in the shallower water. The relationship between L_{w} in the deeper-water region and L_{b} of the FPV patch should be modified accordingly by rewriting the implicit function $F\left(L_{\mathrm{w}}, L_{\mathrm{b}}\right)$ in Eq. (41) as

$$F\left(L_{\mathrm{w}}, L_{\mathrm{b}}\right) = F'_{\mathrm{w}}\left(L_{\mathrm{w}}\right) - F_{\mathrm{b}}\left(L_{\mathrm{b}}\right) = 0, \tag{53}$$

$$F'_{\mathrm{w}}\left(L_{\mathrm{w}}\right) = \frac{L_{\mathrm{w}}}{\tanh\frac{2\pi}{L_{\mathrm{w}}}d_1}. \tag{54}$$

Once the stiffness parameters of the FPV structure have been determined, the resonance conditions shown in Fig. 6 are solely affected by the water depth d_0 below the plate. Therefore, for the present stepped seabed environment, the resonance conditions determined by the ratio of the plate length b and the structural wavelength L_{b} are unchanged. Figure 11 plots the implicit function $F\left(L_{\mathrm{w}}, L_{\mathrm{b}}\right)$ for stepped seabed situations, with d_1/d_0 varying from 1.0 to 2.0. As water waves pass the step,

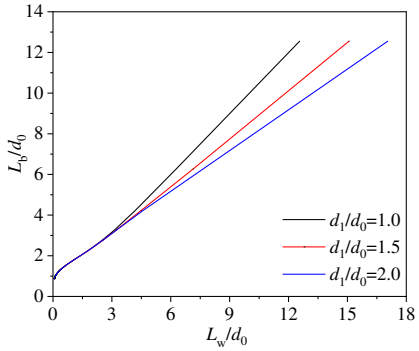

FIG. 11: Implicit function $F(L_w, L_b)$ that forms a one-to-one mapping of L_b and L_w for stepped seabed situations. A larger ratio of d_1/d_0 corresponds to a smaller L'_w, and subsequently a smaller L_b.

the wavelength L_w in the deeper region shrinks to a new wavelength L'_w in the shallower region. A larger water depth ratio of d_1/d_0 corresponds to a smaller wavelength L'_w, and subsequently a smaller structural wavelength L_b.

Figure 12 shows the distribution of the vertical oscillation amplitude along the FPV patch at six resonance conditions, with the water depth ratio d_1/d_0 varying from 1.0 to 2.0. As the height of the step increases, the distributions of the vertical oscillation amplitude of the FPV patch maintain the same pattern, although the maximum oscillation amplitude decreases. Figure 13 shows the variation of the maximum vertical oscillation amplitude of the FPV patch in four resonance conditions, with d_1/d_0 increasing from 1.0 to 1.7. At each resonance condition, the maximum oscillation amplitude decreases as d_1/d_0 increases, because a larger drop causes stronger wave reflection at the edge of the step. As the level of resonance increases from $\zeta = \zeta_1$ to ζ_3, the maximum oscillation amplitude of the FPV patch increases significantly. For resonance conditions above $\zeta = \zeta_3$, the maximum oscillation amplitudes of the FPV patch are almost identical.

E. Effect of adjacent patches on resonance behavior of FPV structure

This subsection focuses on the effect of adjacent patches on the resonance behavior of FPV structures. The FPV structure is formed by two adjacent patches with $D_s = 0$. A plane seabed is considered. Both patches have the same stiffness coefficient $V = 0.005$. The length of Patch-2 is

Accepted to Phys. Fluids 10.1063/5.0169061

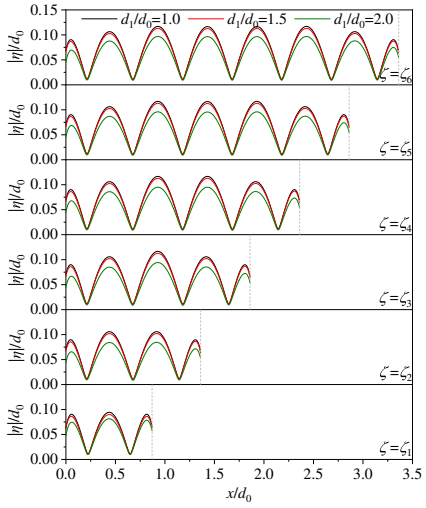

FIG. 12: Distribution of vertical oscillation amplitude of elements along FPV patch at resonance for L_b/d_0 = 1.0 with different seabed step heights. As the height of the step increases, the distributions of the vertical oscillation amplitude of the FPV patch maintain the same pattern, although the maximum oscillation amplitude decreases.

fixed as $b_2 = \zeta_6 d_0$.

Figures 14(a) and 14(b) show the distribution of the maximum oscillation amplitude of elements along Patch-1 and Patch-2, respectively, as the length of Patch-1 varies in different wavelength conditions. As the ratio of b_1/L_b increases to 3.5, Patch-1 experiences a series of resonance conditions at $b_1/L_b = \zeta_1$–ζ_6. The values of ζ_i are identical to those of an isolated FPV patch (see Sec. III B). The existence of Patch-2 enhances the value of b_1/L_b at each resonance condition with increasing L_b/d_0. In other words, the resonance conditions of an FPV patch are slightly affected by the existence of adjacent patches. While maintaining a resonance condition in Patch-1 (e.g., with $b_1/L_b = \zeta_i$), as the water wavelength L_w or elastic wavelength L_b increases, Patch-2 alternates between nonresonance and resonance. The resonance conditions of Patch-2, i.e., $b_2/L_b = \zeta_i$, are also indicated in Fig. 14(a). When the resonance conditions of both patches are satisfied simultaneously, the maximum oscillation amplitude of Patch-1, i.e., the seaward patch, is evidently reduced, but that of the leeward patch (i.e., Patch-2) is still strong.

In the resonance condition of Patch-2 with $b_2/L_b = \zeta_6$, the maximum oscillation amplitudes

Accepted to Phys. Fluids 10.1063/5.0169061

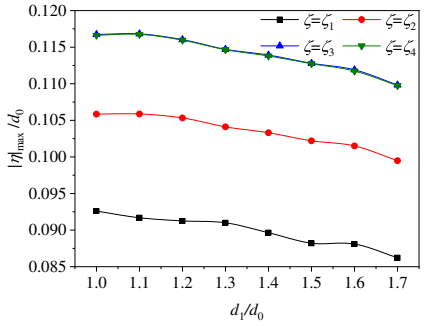

FIG. 13: Maximum vertical oscillation amplitude of FPV elements at four resonance conditions, with d_1/d_0 varying from 1.0 to 1.7. At each resonance condition, the maximum oscillation amplitude decreases as d_1/d_0 increases.

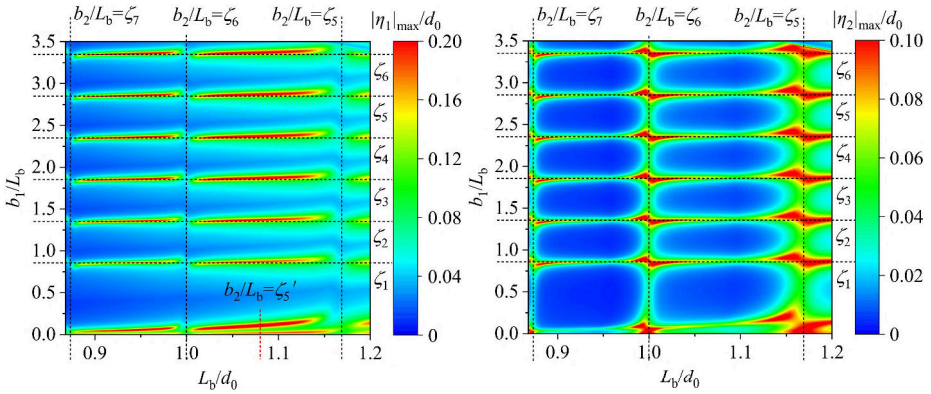

(a) (b)

FIG. 14: Distribution of maximum oscillation amplitude of elements along (a) Patch-1 and (b) Patch-2 as the length of Patch-1 varies in different wavelength conditions. When the resonance conditions of both patches are satisfied simultaneously, the maximum oscillation amplitude of Patch-1, i.e., the seaward patch, is evidently reduced, but that of the leeward patch (i.e., Patch-2) is still strong.

of elements on Patch-1 and Patch-2 are shown in Figs. 15(a) and 15(b), respectively, for Patch-1 lengths from b_1/L_b = 0.5 to 3.5. Figure 15(a) also includes the maximum oscillation amplitude of elements on Patch-1 in the same wave condition without the existence of Patch-2. With and without the existence of Patch-2, Patch-1 always reaches its resonance conditions at around $b_1/L_b = \zeta_i$. Near each resonance condition of Patch-1, the maximum oscillation amplitude of elements on the FPV structure is evidently reduced when Patch-2 exists. A resonant Patch-2 can be considered as wavemaker that radiates waves in both directions. The waves radiated by Patch-2 also satisfy the resonance conditions of Patch-1. Thus, Patch-1 undergoes excitations from both the incident waves and the waves radiated from Patch-2. According to the oscillation amplitude distribution in Fig. 9, the plate waves caused by these two wave groups cancel each other out to some extent. In Fig. 15(b), the maximum oscillation amplitude of elements on an isolated Patch-2 in the same wave condition is shown for reference. With the existence of Patch-1, the maximum oscillation amplitude of Patch-2 at resonance is evidently reduced, mainly because of the wave sheltering effect of Patch-1. Even so, as Patch-1 reaches its resonance conditions, the maximum oscillation amplitude of Patch-2 at resonance is strengthened by the waves radiating from Patch-1.

Figure 16 considers the nonresonance state of Patch-2 with $b_2/L_b = \zeta_5'$. The maximum oscillation amplitude of elements on Patch-1 and Patch-2 versus the length of Patch-1 are given in Figs. 16(a) and 16(b), respectively. With a nonresonant Patch-2, the maximum amplitude of Patch-1 at each resonance condition is amplified by a factor of at least two. The radiation waves generated by Patch-2 strengthen the resonance response amplitude of Patch-1. With a resonant Patch-1 on the seaward side of Patch-2, the maximum oscillation amplitudes of elements on Patch-2 are amplified by a factor of less than two compared with the case of an isolated Patch-2. This suggests that the superposition of radiation waves from Patch-1 and the transmitted waves behind Patch-1 has a larger wave amplitude than the incident waves. Thus, in nonresonance conditions for Patch-2, the resonance of Patch-1 amplifies the maximum oscillation amplitude of Patch-2.

Figure 17(a) shows the distribution of the wave transmission coefficient behind Patch-2 in different wave conditions as the plate length of Patch-1 varies. Comparing Figs. 17(a) and 14 shows that the wave transmission coefficient is positively related to the maximum oscillation amplitude of Patch-2. The transmitted waves of the FPV structure are largely determined by the motion response of the leeward FPV patch. The maximum wave transmission occurs when Patch-1 and Patch-2 resonate at the same time. Figure 17(b) depicts the wave transmission coefficient versus the length of Patch-1 in the resonance condition of Patch-2 with $b_2/L_b = \zeta_6$. As the length of

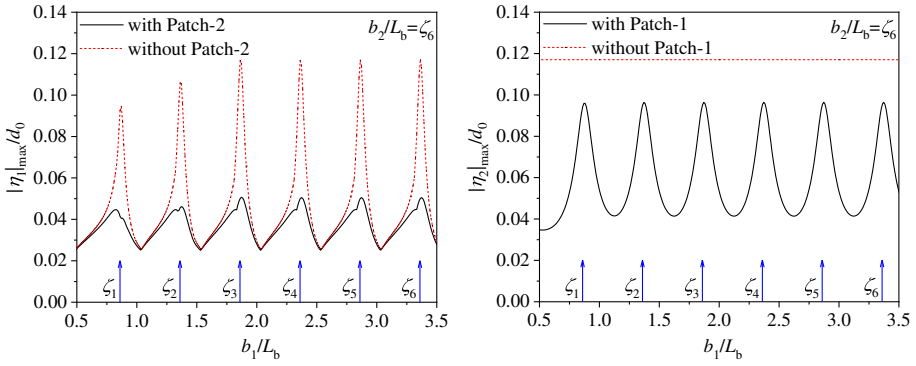

(a) (b)

FIG. 15: With $b_2/L_b = \zeta_6$ as a resonance condition of Patch-2, maximum oscillation amplitudes of elements on (a) Patch-1 and (b) Patch-2 versus length of Patch-1. Maximum oscillation amplitudes of waves on an isolated (a) Patch-1 and (b) Patch-2 in the same wave conditions are also shown. Near each resonance condition of Patch-1, the maximum oscillation amplitude of elements on the FPV structure is evidently reduced when Patch-2 exists. With the existence of Patch-1, the maximum oscillation amplitude of Patch-2 at resonance is evidently reduced.

Patch-1 increases, a series of resonance conditions occur at $b_1/L_b = \zeta_i$, which leads to a maximal wave transmission coefficient at the resonance conditions, regardless of the existence of Patch-2. With a resonant Patch-2 deployed behind Patch-1, the wave transmission coefficient of the FPV structure is amplified at the nonresonance conditions of Patch-1, but is evidently reduced at the resonance conditions.

F. Effect of patch distance on resonance behavior of FPV structure

This subsection further considers the scenario in which Patch-2 is a nonzero distance D_s away from Patch-1. The effect of the gap width between two patches on the resonance behavior of the FPV structure is investigated. The lengths of Patch-1 and Patch-2 are set as $b_1 = b_2 = \zeta_6 d_0$. Hereafter, the symbol b is used to represent the patch lengths. The maximum oscillation amplitudes of elements on Patch-1 and Patch-2 are expressed as $|\eta_1|_{max}$ and $|\eta_2|_{max}$, respectively. The maximum

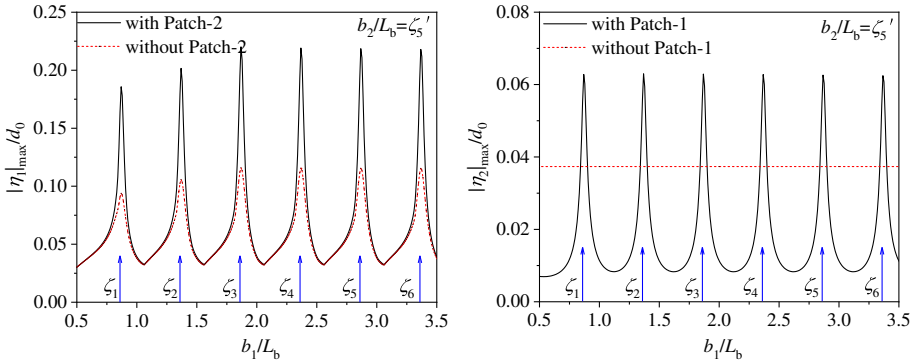

FIG. 16: With $b_2/L_b = \zeta_5'$ as a nonresonance condition of Patch-2, maximum oscillation amplitudes of elements on (a) Patch-1 and (b) Patch-2 versus length of Patch-1. Maximum oscillation amplitudes on an isolated (a) Patch-1 and (b) Patch-2 in the same wave conditions are also shown. With a nonresonant Patch-2, the maximum amplitude of Patch-1 at each resonance condition is amplified by a factor of at least two. In nonresonance conditions for Patch-2, the resonance of Patch-1 amplifies the maximum oscillation amplitude of Patch-2

oscillation amplitude of the water body in the gap is $|\eta_0|_{max}$.

Figures 18(a) and 18(b) show the distribution of the maximum oscillation amplitude of elements along Patch-1 and Patch-2, respectively, as the patch distance varies in different wave conditions. The resonance conditions of $\zeta = \zeta_5$–ζ_7 of the two patches are indicated in both figures. As the distance between the two patches varies, the resonance conditions of each FPV patch do not change. When both patches reach their resonance conditions, the oscillation amplitude of the leeward patch is amplified, but that of the seaward patch is greatly reduced, compared with the behavior of an isolated patch in the same wave conditions. Figure 18(c) gives the distribution of the maximum oscillation amplitude of the water body in the gap. As the ratio of the patch distance D_s and the water wavelength L_w increases up to 5.0, ten resonance states of the water body in the gap appear periodically, near the conditions of $D_s/L_w = \beta_1$ to β_{10}. Here, the values of β are found to be $\beta_1 \approx 0.42$, $\beta_2 \approx 0.92$, $\beta_3 \approx 1.42$, $\beta_4 \approx 1.92$, $\beta_5 \approx 2.42$, $\beta_6 \approx 2.92$, $\beta_7 \approx 3.42$, $\beta_8 \approx 3.92$, $\beta_9 \approx 4.42$, and $\beta_{10} \approx 4.92$. The interval between neighboring values of β is approximately 0.50.

With a fixed patch distance of $D_s = 0.4d_0$ and patch lengths of $b/d_0 = \xi_6$, Fig. 19 shows the

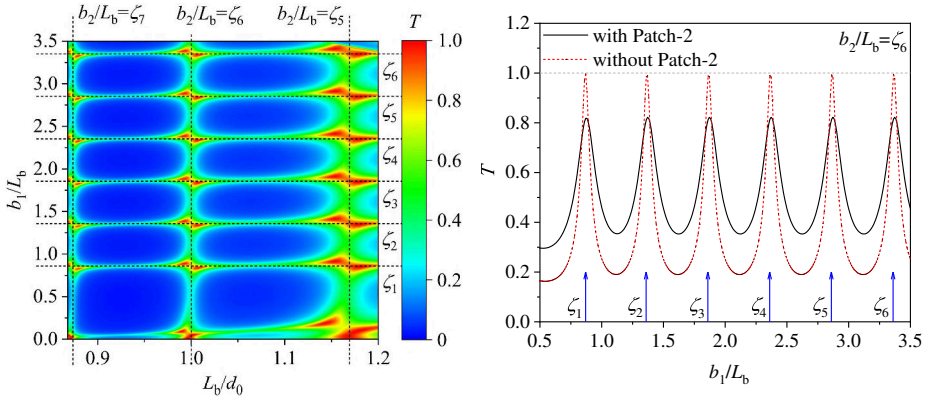

FIG. 17: (a) Distribution of wave transmission coefficient versus dimensionless wavelength and dimensionless plate length of Patch-1 with the existence of Patch-2. (b) Wave transmission coefficient versus plate length of Patch-1 under resonance conditions of Patch-2. With a resonant Patch-2 deployed behind Patch-1, the wave transmission coefficient of the FPV structure is amplified at the nonresonance conditions of Patch-1, but is evidently reduced at the resonance conditions.

distribution of the oscillation amplitudes of elements along Patch-1 and Patch-2, together with the free-surface amplitude in the gap. The incident wave conditions are represented by the ratio b/L_b. As b/L_b increases from 2.8 to 3.8, Patch-1 and Patch-2 both experience three resonance conditions at $b/L_b = \zeta_5$–ζ_7, as denoted by horizontal dashed lines. The interval between two neighboring horizontal dashed lines is $\Delta\zeta$=0.50. In each resonance condition, the oscillation of Patch-1 is evidently weakened compared with the behavior of an isolated Patch-1 in the same wave conditions. The resonance states of the free surface between the two patches can also be determined, although how the free-surface resonance conditions vary with b/L_b is not explicit in Fig. 19. Taking the condition of $b/L_b = \zeta_5$ as an example, the resonance of the two patches increases the amplitude of the constrained free surface that is originally not in a resonance condition.

Figure 20 replots Fig. 19 by converting the ratio of b/L_b to D_s/L_w. The resonance conditions of the water body between the two patches can be identified, i.e., $D_s/L_w = \gamma_i$. As D_s/L_w increases from 1.5 to 6, the resonance conditions of the water body between the two patches sat-

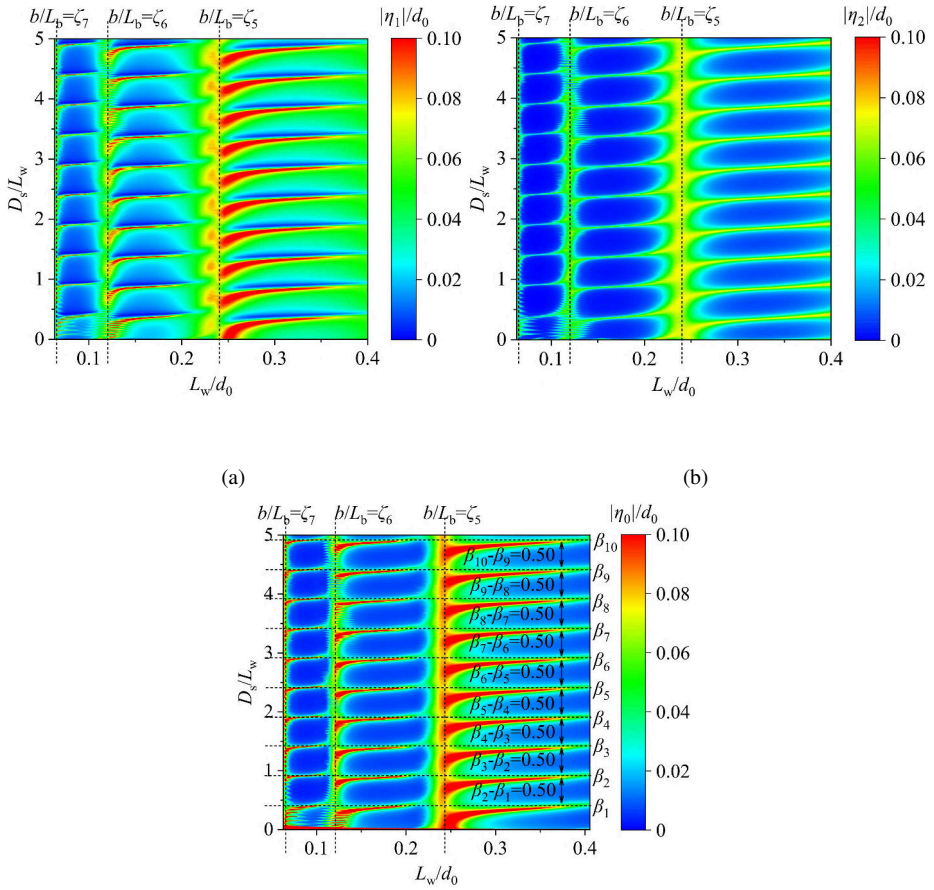

FIG. 18: Distribution of maximum oscillation amplitudes of elements along (a) Patch-1, (b) Patch-2, and (c) water body in the gap for various gap widths and wave conditions. As the distance between the two patches varies, the resonance conditions of each FPV patch do not change. When both patches reach their resonance conditions, the oscillation amplitude of the leeward patch is amplified, but that of the seaward patch is greatly reduced, compared with the behavior of an isolated patch in the same wave conditions.

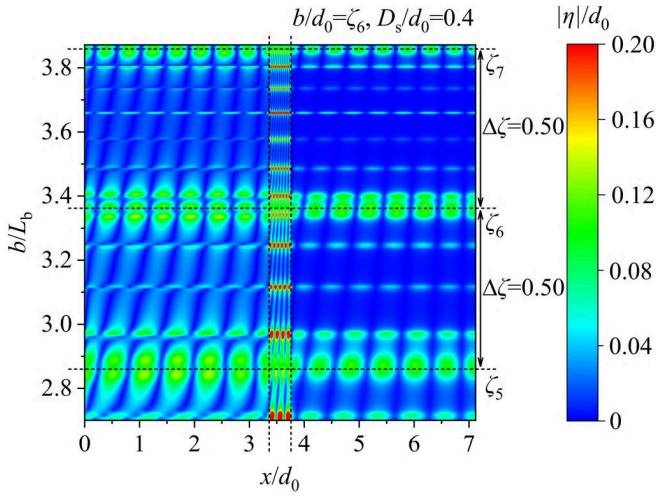

FIG. 19: Oscillation amplitudes of elements along Patch-1 and Patch-2 and of free surface in different wave conditions, with $b/d_0 = \xi_6$, $D_s/D_0 = 0.4$, and wave conditions represented by b/L_b. In each resonance condition, the oscillation of Patch-1 is evidently weakened compared with the behavior of an isolated Patch-1 in the same wave conditions.

isfy $D_s/L_w = \gamma_4$–γ_{10}. In the ordinary condition with two patches, a resonant water body between the patches amplifies the oscillation amplitude of both patches. However, in the special condition of $D_s/L_w = \gamma_7$ (corresponding to $b/L_b = \zeta_6$), the two patches and the water body reach their theoretical resonance conditions at the same time. The resonance of Patch-2 weakens the oscillation amplitude of both Patch-1 and the constrained free surface. Instead, the resonance condition of the water body is split in two around $D_s/L_w = \gamma_7$. Except for the condition of $D_s/L_w = \gamma_7$, the intervals between neighboring resonance conditions of the constrained water body approximately satisfy $D_s/L_w = 0.5$. Moreover, in the resonance condition of $D_s/L_w = \gamma_i$, the oscillation amplitude distribution of the free surface between two patches has i peaks.

IV. CONCLUSIONS

The resonance mechanism of a multi-patch FPV structure in water waves over a stepped seabed has been investigated mathematically. An eigenfunction matching method based on linear potential-flow theory and the thin-plate model was established. An image method based on an

Accepted to Phys. Fluids 10.1063/5.0169061

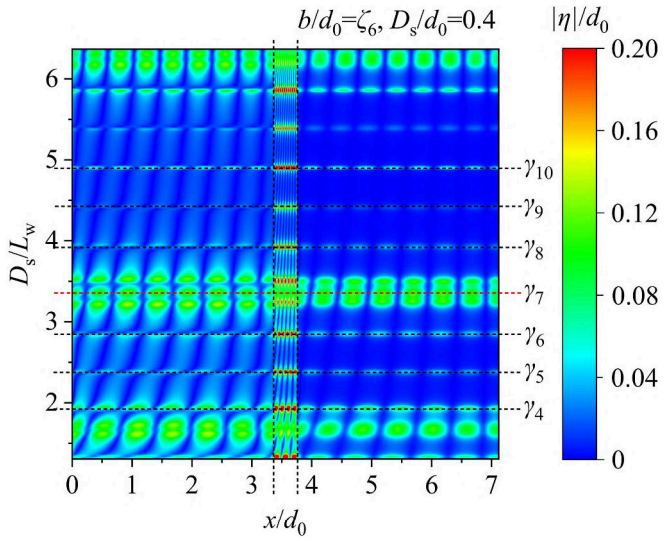

FIG. 20: Oscillation amplitudes of elements along Patch-1 and Patch-2 and of free surface in different wave conditions, with $b/d_0 = \xi_6$, $D_s/D_0 = 0.4$, and wave conditions represented by D_s/L_w. In the ordinary condition with two patches, a resonant water body between the patches amplifies the oscillation amplitude of both patches. However, in the special condition of $D_s/L_w = \gamma_7$ (corresponding to $b/L_b = \zeta_6$), the two patches and the water body reach their theoretical resonance conditions at the same time. The resonance of Patch-2 weakens the oscillation amplitude of both Patch-1 and the constrained free surface.

implicit function was proposed to determine the roots of dispersion equations in the complex domain.

The resonance conditions of an FPV patch were first analyzed. The water bodies with a free surface and an elastic floating plate were considered as two distinct media for propagating waves. As regular waves propagate from open water to the elastic plate, the wave frequency does not change, but the water wavelength is modified to the structural wavelength. The implicit function of the water and structural wavelengths was derived in terms of the water depth below the FPV patch and a dimensionless stiffness parameter. The resonance conditions of the FPV patch are satisfied when the patch length and structural wavelength (rather than the water wavelength) satisfy certain proportions. These proportions form an arithmetic progression with an approximate step of 0.50.

Mathematical derivations were conducted to interpret these values. Two types of resonance conditions, i.e., odd and even conditions, were identified based on the mathematical structure of the solution. Through this process, all possible locations on the FPV patch with the largest oscillation amplitude were identified. The maximum oscillation amplitude was found to appear in the middle of the FPV patch in odd conditions, but away from the middle of the patch in even conditions. In either condition, a resonant FPV patch leads to the maximum wave transmission coefficient.

A stepped seabed was used to investigate the effect of underwater topography on the resonance conditions and hydroelastic behavior of FPV patches. For given stiffness parameters of the FPV patch, the resonance conditions were found to be solely dependent on the water depth below the patch. As the height drop of the stepped seabed increases, the distributions of the vertical oscillation amplitude along the FPV patch maintain the same pattern, but the maximum oscillation amplitude decreases.

For an FPV structure with adjacent patches, the resonance conditions of the FPV patches were observed to be slightly affected by the existence of adjacent patches. The resonance conditions of the seaward patch tend to occur in shorter incident waves compared with the case of an isolated patch. When both patches reach their resonance conditions, the oscillation amplitude of the leeward patch is amplified, but that of the seaward patch is greatly reduced, compared with the behavior of an isolated patch in the same wave conditions. In nonresonance conditions of the leeward patch, the resonance of the seaward patch amplifies the maximum oscillation amplitude of the leeward patch. With a resonant seaward patch, the maximum oscillation amplitude of the leeward patch is amplified by less than a factor of two compared with the case of an isolated patch. The transmitted waves of the FPV structure are largely determined by the motion response of the leeward patch. The maximum wave transmission occurs when both patches resonate at the same time.

The distance between the two patches does not affect the resonance conditions of either patch. The resonance conditions of the water body between the two patches occur when the ratio of the patch distance to the water wavelength satisfies certain proportions. In nonresonance condition of the two patches, a resonant water body between the two patches amplifies the oscillation amplitude of both patches. However, in a special wave condition when the two patches and the water body reach their theoretical resonance conditions at the same time, the oscillation amplitude of both the seaward patch and the constrained free surface are greatly reduced, and the specific resonance

condition of the water body is split in two.

The current mathematical model is based on the linear potential-flow theory with the small wave-amplitude assumption. In practice, an FPV structure may experience nonlinear waves caused by extreme weather events. In a nonlinear-wave environment, the fundamental resonance conditions of the FPV structure are less likely to be severely altered, although the oscillation amplitude of the structure must be reevaluated. In addition, the present FPV structure remains situated in deep waters. If the FPV structure were to be positioned in shallow waters close to the shore, water waves could exhibit significant nonlinear behavior caused by abrupt changes in depth. In that situation, it is important to conduct further analysis on the influence of such nonlinearity on the present findings. Following the work in this study, the nonlinear hydroelastic behavior of a multi-patch FPV structure under resonance in violent waves will be further considered. The two-way coupling fluid-solid interaction algorithm established in Zhang *et al.*[36] can be applied without difficulty.

ACKNOWLEDGMENTS

This study was funded by the Science Foundation of Donghai Laboratory (Grant No. DH-2022KF0309); the National Natural Science Foundation of China (Grant No. U22A20242); the Guangdong Basic and Applied Basic Research Foundation (Grant No. 2022A1515240039); the Special Project of Guangdong Science and Technology Department (Grant No. 2021A05227); and the Fundamental Research Funds for the Central Universities (Grant No. DUT22LAB128).

Appendix A: Introduction of dispersion equations

This section provides a concise introduction of dispersion equations, intended for readers who may lack familiarity with the subject matter. According to the assumption of the method of variable separation, the spatial potential $\phi^{(j)}$ is expressed as

$$\phi^{(j)}(x,z) = X^{(j)}(x)Z^{(j)}(z) \tag{A1}$$

Substituting Eq. (A1) into Eq. (2) leads to

$$\frac{1}{X^{(j)}(x)}\frac{\partial^2 X^{(j)}(x)}{\partial x^2} = -\frac{1}{Z^{(j)}(z)}\frac{\partial^2 Z^{(j)}(z)}{\partial z^2} \tag{A2}$$

Since the expressions on the left and right side of Eq. (A2) are dependent to x and z, respectively, both expressions should be some constant (e.g. λ).

All possible solutions of the second-order linear differential equations in the function $X^{(j)}$ and $Z^{(j)}$ can be expressed as

$$\begin{cases} X^{(j)}(x) = Ae^{ik^{(j)}x} + Be^{-ik^{(j)}x} \\ Z^{(j)}(z) = Ce^{k^{(j)}z} + De^{-k^{(j)}z} \end{cases}, \text{ for } \lambda < 0, \tag{A3}$$

$$\begin{cases} X^{(j)}(x) = A + Bx \\ Z^{(j)}(z) = C + Dz \end{cases}, \text{ for } \lambda = 0, \tag{A4}$$

and

$$\begin{cases} X^{(j)}(x) = Ae^{\kappa^{(j)}x} + Be^{-\kappa^{(j)}x} \\ Z^{(j)}(z) = Ce^{i\kappa^{(j)}z} + De^{-i\kappa^{(j)}z} \end{cases} \text{ for } \lambda > 0. \tag{A5}$$

where A_1, B_1, C_1, D_1, A_2, B_2, C_2, D_2, A_3, B_3, C_3, D_3, k and κ are all undetermined coefficients. By substituting Eq. (A3) – (A5) into Eq. (A1), the spatial potential can be expressed as

$$\phi^{(j)}(x,z) = \begin{cases} \left(A_1e^{ik^{(j)}x} + B_1e^{-ik^{(j)}x}\right)\left[C_1e^{k^{(j)}z} + D_1e^{-k^{(j)}z}\right], \text{ for } \lambda < 0 \\ (A_2 + B_2x)(C_2 + D_2z), \text{ for } \lambda = 0 \\ \left(A_3e^{\kappa^{(j)}x} + B_3e^{-\kappa^{(j)}x}\right)\left[C_3e^{i\kappa^{(j)}z} + D_3e^{-i\kappa^{(j)}z}\right], \text{ for } \lambda > 0 \end{cases} \tag{A6}$$

or

$$\phi^{(j)}(x,z) = \begin{cases} \left(A_1e^{ik^{(j)}x} + B_1e^{-ik^{(j)}x}\right)\left[C_1\cosh k^{(j)}(z+h) + D_1\sinh k^{(j)}(z+h)\right], \text{ for } \lambda < 0 \\ (A_2 + B_2x)(C_2 + D_2z), \text{ for } \lambda = 0 \\ \left(A_3e^{\kappa^{(j)}x} + B_3e^{-\kappa^{(j)}x}\right)\left[C_3\cos\kappa^{(j)}(z+d) + D_3\sin\kappa^{(j)}(z+d)\right], \text{ for } \lambda > 0 \end{cases}. \tag{A7}$$

Substituting Eq. (A7) into the bottom condition Eq. (3) , it becomes

$$\begin{cases} \left(A_1e^{ik^{(j)}x} + B_1e^{-ik^{(j)}x}\right)D_1k^{(j)} = 0, \text{ for } \lambda < 0 \\ (A_2 + B_2x)D_2 = 0, \text{ for } \lambda = 0 \\ \left(A_3e^{\kappa^{(j)}x} + B_3e^{-\kappa^{(j)}x}\right)D_3\kappa^{(j)} = 0, \text{ for } \lambda > 0 \end{cases} \tag{A8}$$

Since the functions of x should not be constant zero, it has $D_1 = D_2 = D_3 = 0$. Eq. (A7) can be

simplified as

$$\phi^{(j)}(x,z)=\begin{cases}\left(A_1e^{ik^{(j)}x}+B_1e^{-ik^{(j)}x}\right)C_1\cosh k^{(j)}(z+h), & \text{for } \lambda<0\\ (A_2+B_2x)C_2, & \text{for } \lambda=0\\ \left(A_3e^{\kappa^{(j)}x}+B_3e^{-\kappa^{(j)}x}\right)C_3\cos\kappa^{(j)}(z+d), & \text{for } \lambda>0\end{cases} \tag{A9}$$

Further substituting Eq. (A9) into the free-surface BC Eq. (7) leads to

$$\left(A_1e^{ik_0^{(j)}x}+B_1e^{-ik_0^{(j)}x}\right)\left(k_0^{(j)}\sinh k_0^{(j)}d-\frac{\omega^2}{g}\cosh k_0^{(j)d}\right)=0 \tag{A10}$$

$$-(A_2+B_2x)\frac{\omega^2}{g}C_2=0 \tag{A11}$$

$$\left(A_3e^{k_m^{(j)}x}+B_3e^{-k_m^{(j)}x}\right)\left(-k_m^{(j)}\sin k_m^{(j)}d-\frac{\omega^2}{g}\cos k_m^{(j)}d\right)=0 \tag{A12}$$

To guarantee the solvability of Eq. (A10) – (A12), it requires $C_2=0$ and

$$\omega^2=gk_0^{(j)}\tanh k_0^{(j)}d^{(j)} \tag{A13}$$

$$\omega^2=-gk_m^{(j)}\tan k_m^{(j)}d^{(j)}. \tag{A14}$$

This is how the dispersion equations of Eqs. (22) and (23) are obtained.

Similarly, substituting Eq.(A9) into the plate-surface BC Eq. (9) leads to

$$\left(A_1e^{i\lambda_0^{(j)}x}+B_1e^{-i\lambda_0^{(j)}x}\right)\left[\lambda_0^{(j)}\sinh\lambda_0^{(j)}d\left(K\left(\lambda_0^{(j)}\right)^4+W\right)-\cosh\lambda_0^{(j)}d\right]=0 \tag{A15}$$

$$-(A_2+B_2x)C_2=0 \tag{A16}$$

$$\left(A_3e^{\lambda_n^{(j)}x}+B_3e^{-\lambda_n^{(j)}x}\right)\left[-\lambda_n^{(j)}\sin\lambda_n^{(j)}d\left(K\left(\lambda_n^{(j)}\right)^4+W\right)-\cos\lambda_n^{(j)}d\right]=0 \tag{A17}$$

It requires $C_2=0$ and

$$\lambda_0^{(j)}\left(K\left(\lambda^{(j)}\right)^4+W\right)\tanh\lambda_0^{(j)}d_0=1 \tag{A18}$$

$$-\lambda_n^{(j)}\left(K\left(\lambda_n^{(j)}\right)^4+W\right)\tan\lambda_n^{(j)}d_0=1. \tag{A19}$$

This is how Eqs. (24) and (25) are obtained.

Appendix B: Solution of dispersion equations

This section describes the procedure for determining the solution of the following dispersion equations:

$$k\left(Kk^4+W\right)\tanh kd=1, \tag{B1}$$

$$\omega^2=gk\tanh kd, \tag{B2}$$

$$-\kappa\left(K\kappa^4+W\right)\tan\kappa d=1, \tag{B3}$$

$$\omega^2=-g\kappa\tan\kappa d. \tag{B4}$$

Equations (B1) and (B2) have only one positive real root, which can be solved using Newton's method. However, Eqs. (B3) and (B4) have complex roots, which should be treated carefully.

An image method based on an implicit function is used to seek the roots of Eq. (B3). The solution κ can be expressed as $\kappa=a_3+b_3\mathrm{i}$, and Eq. (B3) becomes

$$(a_3+b_3\mathrm{i})\left[K(a_3+b_3\mathrm{i})^4+W\right]\tan(a_3+b_3\mathrm{i})d_0+1=0. \tag{B5}$$

Expanding Eq. (B5) yields

$$(a_4b_4-a_5b_5+a_6)+(a_4b_5+a_5b_4+b_6)\mathrm{i}=0 \tag{B6}$$

with

$$\begin{aligned}
a_4&=Ka_3^5-6Ka_3^3b_3^2+Ka_3b_3^4-4Ka_3^3b_3^2+4Ka_3b_3^4+a_3W,\\
a_5&=4Ka_3^4b_3-4Ka_3^2b_3^3+Ka_3^4b_3-6Ka_3^2b_3^3+Kb_3^5+b_3W,\\
a_6&=\left(e^{-b_3d_0}+e^{b_3d_0}\right)\cos a_3d_0,\\
b_4&=\left(e^{-b_3d_0}+e^{b_3d_0}\right)\sin a_3d_0,\\
b_5&=\left(e^{b_3d_0}-e^{-b_3d_0}\right)\cos a_3d_0,\\
b_6&=\left(e^{-b_3d_0}-e^{b_3d_0}\right)\sin a_3d_0.
\end{aligned} \tag{B7}$$

Therefore, we have

$$\begin{cases} f_1(a_3,b_3)=a_4b_4-a_5b_5+a_6=0,\\ f_2(a_3,b_3)=a_4b_5-a_5b_4+b_6=0. \end{cases} \tag{B8}$$

The implicit functions of $f_1(a_3,b_3)=0$ and $f_2(a_3,b_3)=0$ can be plotted on the same image, forming two groups of curves. Among the intersection points of these two groups of curves, those with $a_3>0$ determine the roots of Eq. (B3).

Similarly, substituting $\kappa = a_7 + b_7\mathrm{i}$ into Eq. (B4) yields

$$\omega^2 + g(a_7 + \mathrm{i}b_7)\tan(a_7 + \mathrm{i}b_7) = 0, \tag{B9}$$

i.e.,

$$(a_8 - a_9 + a_{10}) + \mathrm{i}(b_8 + b_9 + b_{10}) = 0 \tag{B10}$$

with

$$\begin{aligned}
a_8 &= g a_7 \left(e^{-b_7 d} + e^{b_7 d}\right)\sin a_7 d,\\
a_9 &= g b_7 \left(e^{b_7 d} - e^{-b_7 d}\right)\cos a_7 d,\\
a_{10} &= \omega^2 \left(e^{-b_7 d} + e^{b_7 d}\right)\cos a_7 d,\\
b_8 &= g b_7 \left(e^{-b_7 d} + e^{b_7 d}\right)\sin a_7 d,\\
b_9 &= g a_7 \left(e^{b_7 d} - e^{-b_7 d}\right)\cos a_7 d,\\
b_{10} &= \omega^2 \left(e^{-b_7 d} - e^{b_7 d}\right)\sin a_7 d.
\end{aligned} \tag{B11}$$

The following pair of implicit functions can be obtained:

$$\begin{cases} f_3(a_7, b_7) = a_8 - a_9 + a_{10} = 0, \\ f_4(a_7, b_7) = b_8 + b_9 + b_{10} = 0. \end{cases} \tag{B12}$$

The intersection points of $f_3(a_7, b_7) = 0$ and $f_4(a_7, b_7) = 0$ can be detected on the same image, and those with $a_7 > 0$ give the roots of Eq. (B4).

A specific case with parameters of $d = 10\mathrm{m}$, $E = 6 \times 10^9\mathrm{Pa}$, $c = 1\mathrm{m}$, $\nu = 0.38$, $g = 9.81\mathrm{m/s^2}$, $\rho = 1025\mathrm{kg/m^3}$, $\rho_s = 950\mathrm{kg/m^3}$, and the incident wavelength $L_\mathrm{w} = 100\mathrm{m}$ is taken as an example. Figure 21(a) shows the curves of $f_1(a_3, b_3) = 0$ (in black) and $f_2(a_3, b_3) = 0$ (in red). The intersection points of the black and red lines with $a_3 > 0$ are λ_j. Note that λ_1 and λ_2 are complex conjugates, and λ_n ($n > 2$) is on the positive real axis. Figure 21(b) shows $f_3(a_7, b_7) = 0$ (in black) and $f_4(a_7, b_7) = 0$ (in red). Their intersection points with $a_7 > 0$ are k_m.

Appendix C: Matching of interface conditions

The orthogonal relationship among the vertical eigenfunctions can be used to simplify the matching conditions on each interface. Taking the interface at $x = 0$ as an example, the following matching conditions are satisfied:

$$<< \phi^{(2)}, Y_n^{(2)} >>_{-d_0}^{0} - K\left\{\frac{\partial \phi^{(2)}}{\partial z}\frac{\partial^3 Y_n^{(2)}}{\partial z^3} + \frac{\partial^3 \phi^{(2)}}{\partial z^3}\frac{\partial Y_n^{(2)}}{\partial z}\right\}_{z=0} = < \phi^{(1)}, Y_n^{(2)} >_{-d_0}^{0}, \tag{C1}$$

$$< \frac{\partial \phi^{(2)}}{\partial x}, Z_m^{(1)} >_{-d_0}^{0} = < \frac{\partial \phi^{(1)}}{\partial x}, Z_m^{(1)} >_{-d_1}^{0}. \tag{C2}$$

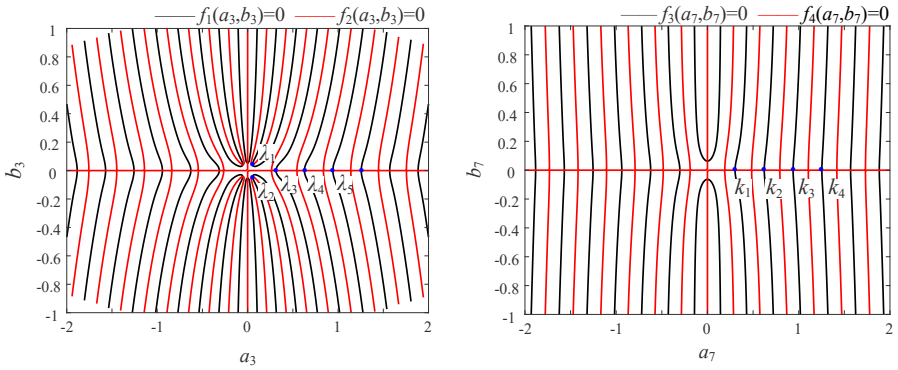

(a) (b)

FIG. 21: Distribution of the roots of the dispersion equation (a) beneath the elastic plate and (b) beneath the open water.

Combining the free-end condition in Eq. (10) with the Laplace equation leads to the relationship

$$\frac{\partial^3\phi^{(2)}}{\partial z^3}=0 \text{ and } \frac{\partial^4\phi^{(2)}}{\partial x^3\partial z}=0 \text{ for } x=0 \text{ and } z=0. \tag{C3}$$

In the case of $n=0$ or $m=0$, the following expressions can be obtained:

$$<<\phi^{(2)},Y_0^{(2)}>>_{-d_0}^{0}=-\frac{igA}{\omega}\left[\left(A_0+B_0e^{i\lambda_0^{(2)}b_1}\right)<<Y_0^{(2)},Y_0^{(2)}>>_{-d_0}^{0}\right], \tag{C4}$$

$$\left\{\frac{\partial\phi^{(2)}}{\partial z}\frac{\partial^3Y_0^{(2)}}{\partial z^3}\right\}_{z=0}=-\frac{igA}{\omega}\left[\begin{array}{l}\left(A_0+B_0e^{i\lambda_0^{(2)}b_1}\right)\left(\lambda_0^{(2)}\right)^4\tanh^2\lambda_0^{(2)}d_0\\-\sum_{n=1}^{\infty}\left(A_n+B_ne^{-\lambda_n^{(2)}b_1}\right)\left(\lambda_0^{(2)}\right)^3\tanh\lambda_0^{(2)}d_0\lambda_n^{(2)}\tan\lambda_n^{(2)}d_0\end{array}\right], \tag{C5}$$

$$<\phi^{(1)},Y_0^{(2)}>_{-d_0}^{0}=-\frac{igA}{\omega}\left[\begin{array}{l}\int_{-d_0}^{0}Z_0^{(1)}Y_0^{(2)}dz\\+\int_{-d_0}^{0}\sum_{m=0}^{\infty}R_mZ_m^{(1)}Y_0^{(2)}dz\end{array}\right], \tag{C6}$$

$$<\frac{\partial\phi^{(2)}}{\partial x},Z_0^{(1)}>_{-d_0}^{0}=-\frac{igA}{\omega}\int_{-d_0}^{0}\left[\begin{array}{l}\left(i\lambda_0^{(2)}A_0-i\lambda_0^{(2)}e^{i\lambda_0^{(2)}b_1}B_0\right)Y_0^{(2)}\\+\sum_{n=1}^{\infty}\left(-\lambda_n^{(2)}A_n+\lambda_n^{(2)}e^{-\lambda_n^{(2)}b_1}B_n\right)Y_0^{(2)}\end{array}\right]Z_0^{(1)}dz, \tag{C7}$$

$$<\frac{\partial\phi^{(1)}}{\partial x},Z_0^{(1)}>_{-d_1}^{0}=-\frac{igA}{\omega}\int_{-d_1}^{0}\left[\left(ik_0^{(1)}-ik_0^{(1)}R_0\right)\left(Z_0^{(1)}\right)^2\right]dz. \tag{C8}$$

In the case of $n > 0$ or $m > 0$, we have

$$<< \phi^{(2)}, Y_n^{(2)} >>_{-d_0}^{0} = -\frac{igA}{\omega}\left[\left(A_n + B_n e^{-\lambda_n^{(2)} b_1}\right) << Y_n^{(2)}, Y_n^{(2)} >>_{-d_0}^{0}\right], \tag{C9}$$

$$\left\{\frac{\partial \phi^{(2)}}{\partial z}\frac{\partial^3 Y_n^{(2)}}{\partial z^3}\right\}_{z=0} = -\frac{igA}{\omega}\left\{\begin{array}{l}(A_0 + B_0 e^{i\lambda_0^{(2)} b_1})\lambda_0^{(2)} \tanh \lambda_0^{(2)} d_0 \left(\lambda_n^{(2)}\right)^3 \tan \lambda_n^{(2)} d_0 \\ -\left[\sum_{n=1}^{\infty}(A_n + B_n e^{-\lambda_n b_1})\lambda_n^{(2)} \tan \lambda_n^{(2)} d_0\right]\left(\lambda_n^{(2)}\right)^3 \tan \lambda_n^{(2)} d_0\end{array}\right\}, \tag{C10}$$

$$< \phi^{(1)}, Y_n^{(2)} >_{-d_0}^{0} = -\frac{igA}{\omega}\left[\begin{array}{l}\int_{-d_0}^{0} Z_0^{(1)} Y_n^{(2)} dz \\ +\int_{-d_0}^{0} \sum_{m=0}^{\infty} R_m Z_m^{(1)} Y_n^{(2)} dz\end{array}\right], \tag{C11}$$

$$< \frac{\partial \phi^{(2)}}{\partial x}, Z_m^{(1)} >_{-d_0}^{0} = -\frac{igA}{\omega}\int_{-d_0}^{0}\left[\begin{array}{l}\left(i\lambda_0^{(2)} A_0 - i\lambda_0^{(2)} e^{i\lambda_0^{(2)} b_1} B_0\right) Y_0^{(2)} \\ +\sum_{n=1}^{\infty}\left(-\lambda_n^{(2)} A_n + \lambda_n^{(2)} e^{-\lambda_n^{(2)} b_1} B_n\right) Y_n^{(2)}\end{array}\right] Z_m^{(1)} dz, \tag{C12}$$

$$< \frac{\partial \phi^{(1)}}{\partial x}, Z_m^{(1)} >_{-d_1}^{0} = -\frac{igA}{\omega}\int_{-d_1}^{0} R_m k_m^{(1)} \left(Z_m^{(1)}\right)^2 dz. \tag{C13}$$

Appendix D: Establishment of linear equations

By truncating the series expansions of ϕ_1 in Eq. (17) and ϕ_2 in Eq. (18) after M and N terms, respectively, Eqs. (C1) and (C2) become

$$\begin{array}{l}\left[a_{nn}^{(1)}\right]_{(N+1)\times(N+1)}\{A_n\}_{(N+1)} + \left[b_{nn}^{(1)}\right]_{(N+1)\times(N+1)}\{B_n\}_{(N+1)} \\ + \left[c_{nn}^{(1)}\right]_{(N+1)\times(N+1)}\{A_n\}_{(N+1)} + \left[d_{nn}^{(1)}\right]_{(N+1)\times(N+1)}\{B_n\}_{(N+1)} \\ = \left\{f_n^{(1)}\right\}_{(N+1)} + \left[p_{nm}^{(1)}\right]_{(N+1)\times(M+1)}\{R_m\}_{(M+1)} \text{ for } m = 1, 2, 3, \cdots, M\end{array} \tag{D1}$$

and

$$\begin{array}{l}\left[q_{mn}^{(1)}\right]_{(M+1)\times(N+1)}\{A_n\}_{(N+1)} + \left[r_{mn}^{(1)}\right]_{(M+1)\times(N+1)}\{B_n\}_{(N+1)} \\ = \{e_m\}_{(M+1)} + \{R_m\}_{(M+1)} \text{ for } m = 1, 2, 3, \cdots, M,\end{array} \tag{D2}$$

where $e_0 = -1$, $e_m = 0$; the elements of each matrix are derived in Appendix E. The superscript (j) in the elements of matrices refers to the matching conditions on the interface between V_j and $V_{(j+1)}$. This study takes $M = 40$ to guarantee the convergence of the numerical results. Similarly, applying the matching conditions on the interfaces at $x = b_1$, a_1, and a_2 leads to the following sets

of linear equations:

$$\left[b_{nn}^{(2)}\right]_{(N+1)\times(N+1)}\{A_n\}_{(N+1)}+\left[a_{nn}^{(2)}\right]_{(N+1)\times(N+1)}\{B_n\}_{(N+1)} +\left[d_{nn}^{(2)}\right]_{(N+1)\times(N+1)}\{A_n\}_{(N+1)}+\left[c_{nn}^{(2)}\right]_{(N+1)\times(N+1)}\{B_n\}_{(N+1)} =\left\{p_{nm}^{(2)}\right\}_{(N+1)\times(M+1)}\{C_m\}_{(M+1)}+\left\{u_{nm}^{(2)}\right\}_{(N+1)\times(M+1)}\{D_m\}_{(M+1)}, \tag{D3}$$

$$\left[r_{mn}^{(2)}\right]_{(M+1)\times(N+1)}\{A_n\}_{(N+1)}+\left[q_{mn}^{(2)}\right]_{(M+1)\times(N+1)}\{B_n\}_{(N+1)} =\{C_m\}_{(M+1)}-\left\{v_{mm}^{(2)}\right\}_{(M+1)\times(M+1)}\{D_m\}_{(M+1)}, \tag{D4}$$

$$\left[u_{nm}^{(3)}\right]_{(N+1)\times(M+1)}\{C_m\}_{(M+1)}+\left[p_{nm}^{(3)}\right]_{(N+1)\times(M+1)}\{D_m\}_{(M+1)} =\left[a_{nn}^{(3)}\right]_{(N+1)\times(N+1)}\{E_n\}_{(N+1)}+\left[B_{nn}^{(3)}\right]_{(N+1)\times(N+1)}\{F_n\}_{(N+1)} +\left\{c_{nn}^{(3)}\right\}_{(N+1)\times(N+1)}\{E_n\}_{(N+1)}+\left\{D_{nn}^{(3)}\right\}_{(N+1)\times(N+1)}\{F_n\}_{(N+1)}, \tag{D5}$$

$$\left[-v_{mm}^{(3)}\right]_{(M+1)\times(M+1)}\{C_m\}_{(M+1)}-\{D_m\}_{(M+1)} =\left[q_{mn}^{(3)}\right]_{(M+1)\times(N+1)}\{E_n\}_{(N+1)}+\left[R_{mn}^{(3)}\right]_{(M+1)\times(N+1)}\{F_n\}_{(N+1)} \tag{D6}$$

$$\left[B_{nn}^{(4)}\right]_{(N+1)\times(N+1)}\{E_n\}_{(N+1)}+\left[a_{nn}^{(4)}\right]_{(N+1)\times(N+1)}\{F_n\}_{(N+1)} +\left[D_{nn}^{(4)}\right]_{(N+1)\times(N+1)}\{E_n\}_{(N+1)}+\left[c_{nn}^{(4)}\right]_{(N+1)\times(N+1)}\{F_n\}_{(N+1)} =\left\{p_{nm}^{(4)}\right\}_{(N+1)\times(M+1)}\{T_m\}_{(M+1)}, \tag{D7}$$

$$\left[R_{mn}^{(4)}\right]_{(M+1)\times(N+1)}\{E_n\}_{(N+1)}+\left[q_{mn}^{(4)}\right]_{(M+1)\times(N+1)}\{F_n\}_{(N+1)} =\{T_m\}_{(M+1)}. \tag{D8}$$

By letting $M = N$, the following system of linear equations can be obtained:

$$[J]_{8(N+1)\times 8(N+1)}\{X\}_{8(N+1)}=\{K\}_{8(N+1)} \tag{D9}$$

with

$$[J]=\begin{bmatrix} H & I \\ P & Q \end{bmatrix}, \tag{D10}$$

$$[H]=\begin{bmatrix} a_{nn}^{(1)}+c_{nn}^{(1)} & b_{nn}^{(1)}+d_{nn}^{(1)} & O_{nn} & O_{nn} \\ q_{mn}^{(1)} & r_{mn}^{(1)} & O_{nn} & O_{nn} \\ b_{nn}^{(2)}+d_{nn}^{(2)} & a_{nn}^{(2)}+c_{nn}^{(2)} & -p_{nm}^{(2)} & -u_{nm}^{(2)} \\ r_{mn}^{(2)} & q_{mn}^{(2)} & U_{nn} & v_{mm}^{(2)} \end{bmatrix}, \tag{D11}$$

$$[I]=\begin{bmatrix} O_{nn} & O_{nn} & -p_{nm}^{(1)} & O_{nn} \\ O_{nn} & O_{nn} & U_{nn} & O_{nn} \\ O_{nn} & O_{nn} & O_{nn} & O_{nn} \\ O_{nn} & O_{nn} & O_{nn} & O_{nn} \end{bmatrix}, \tag{D12}$$

$$[P]=\begin{bmatrix} O_{nn} & O_{nn} & u_{nm}^{(3)} & p_{nm}^{(3)} \\ O_{nn} & O_{nn} & -v_{mm}^{(3)} & -U_{nn} \\ O_{nn} & O_{nn} & O_{nn} & O_{nn} \\ O_{nn} & O_{nn} & O_{nn} & O_{nn} \end{bmatrix}, \tag{D13}$$

$$[Q]=\begin{bmatrix} -(a_{nn}^{(3)}+c_{nn}^{(3)}) & -(B_{nn}^{(3)}+D_{nn}^{(3)}) & O_{nn} & O_{nn} \\ -q_{mn}^{(3)} & -R_{mn}^{(3)} & O_{nn} & O_{nn} \\ B_{nn}^{(4)}+D_{nn}^{(4)} & a_{nn}^{(4)}+c_{nn}^{(4)} & O_{nn} & -p_{nm}^{(4)} \\ R_{mn}^{(4)} & q_{mn}^{(4)} & O_{nn} & U_{nn} \end{bmatrix}, \tag{D14}$$

$$\{X\}=\{A_n,B_n,C_m,D_m,E_n,F_n,R_m,T_m\}^T, \tag{D15}$$

$$\{K\}=\left\{f_n^{(1)},e_m,W_n,W_n,W_n,W_n,W_n,W_n\right\}^T, \tag{D16}$$

$$\{O_{nn}\}=\begin{bmatrix} 0 & 0 & \cdots & 0 \\ 0 & 0 & \cdots & 0 \\ \cdots & \cdots & \cdots & \cdots \\ 0 & 0 & \cdots & 0 \end{bmatrix}_{(N+1)\times(N+1)}, \tag{D17}$$

$$[U_{nn}]=\begin{bmatrix} -1 & 0 & \ldots & 0 \\ 0 & -1 & \ldots & 0 \\ \ldots & \ldots & \ldots & \ldots \\ 0 & 0 & \ldots & -1 \end{bmatrix}_{(N+1)\times(N+1)}, \tag{D18}$$

$$[W_n]=[0,0\cdots 0]_{(N+1)}^T \tag{D19}$$

The unknown coefficients can be obtained by solving the system of linear equations.

Appendix E: Coefficients in system of linear equations

The coefficients of the system of linear equations in Sec. D are derived as follows.

$$\begin{aligned} a_{00}^{(1)} &= \frac{2\lambda_0^{(2)}d_0+\sinh 2\lambda_0^{(2)}d_0+8K\left(\lambda_0^{(2)}\right)^5\sinh^2\lambda_0^{(2)}d_0}{4\lambda_0^{(2)}\cosh^2\lambda_0^{(2)}d_0} \\ a_{nn}^{(1)} &= \frac{2\lambda_n^{(2)}d_0+\sin 2\lambda_n^{(2)}d_0-8K\left(\lambda_n^{(2)}\right)^5\sin^2\lambda_n^{(2)}d_0}{4\lambda_n^{(2)}\cos^2\lambda_n^{(2)}d_0} \end{aligned} \tag{E1}$$

$$\begin{aligned} a_{00}^{(2)} &= \frac{2\lambda_0^{(2)}d_0+\sinh 2\lambda_0^{(2)}d_0+8K\left(\lambda_0^{(2)}\right)^5\sinh^2\lambda_0^{(2)}d_0}{4\lambda_0^{(2)}\cosh^2\lambda_0^{(2)}d_0} \\ a_{nn}^{(2)} &= \frac{2\lambda_n^{(2)}d_0+\sin 2\lambda_n^{(2)}d_0-8K\left(\lambda_n^{(2)}\right)^5\sin^2\lambda_n^{(2)}d_0}{4\lambda_n^{(2)}\cos^2\lambda_n^{(2)}d_0} \end{aligned} \tag{E2}$$

$$\begin{aligned} a_{00}^{(3)} &= \frac{2\lambda_0^{(4)}d_0+\sinh 2\lambda_0^{(4)}d_0+8K\left(\lambda_0^{(4)}\right)^5\sinh^2\lambda_0^{(4)}d_0}{4\lambda_0^{(4)}\cosh^2\lambda_0^{(4)}d_0} \\ a_{nn}^{(3)} &= \frac{2\lambda_n^{(4)}d_0+\sin 2\lambda_n^{(4)}d_0-8K\left(\lambda_n^{(4)}\right)^5\sin^2\lambda_n^{(4)}d_0}{4\lambda_n^{(4)}\cos^2\lambda_n^{(4)}d_0} \end{aligned} \tag{E3}$$

$$\begin{aligned} a_{00}^{(4)} &= \frac{2\lambda_0^{(4)}d_0+\sinh 2\lambda_0^{(4)}d_0+8K\left(\lambda_0^{(4)}\right)^5\sinh^2\lambda_0^{(4)}d_0}{4\lambda_0^{(4)}\cosh^2\lambda_0^{(4)}d_0} \\ a_{nn}^{(4)} &= \frac{2\lambda_n^{(4)}d_0+\sin 2\lambda_n^{(4)}d_0-8K\left(\lambda_n^{(4)}\right)^5\sin^2\lambda_n^{(4)}d_0}{4\lambda_n^{(4)}\cos^2\lambda_n^{(4)}d_0} \end{aligned} \tag{E4}$$

$$\begin{aligned} b_{00}^{(1)} &= e^{\mathrm{i}\lambda_0^{(2)}b_1}a_{00}^{(1)} \\ b_{nn}^{(1)} &= e^{-\lambda_n^{(2)}b_1}a_{nn}^{(1)} \end{aligned} \tag{E5}$$

$$\begin{aligned} b_{00}^{(2)} &= e^{\mathrm{i}\lambda_0^{(2)}b_1}a_{00}^{(2)} \\ b_{nn}^{(2)} &= e^{-\lambda_n^{(2)}b_1}a_{nn}^{(2)} \end{aligned} \tag{E6}$$

$$\begin{aligned} B_{00}^{(3)} &= e^{\mathrm{i}\lambda_0^{(4)}b_2}a_{00}^{(3)} \\ B_{nn}^{(3)} &= e^{-\lambda_n^{(4)}b_2}a_{nn}^{(3)} \end{aligned} \tag{E7}$$

$$\begin{aligned} B_{00}^{(4)} &= e^{\mathrm{i}\lambda_0^{(4)}b_2}a_{00}^{(4)} \\ B_{nn}^{(4)} &= e^{-\lambda_n^{(4)}b_2}a_{nn}^{(4)} \end{aligned} \tag{E8}$$

$$\begin{aligned} c_{00}^{(1)} &= -K\left(\lambda_0^{(2)}\right)^4\tanh^2\lambda_0^{(2)}d_0 \\ c_{0n}^{(1)} &= K\left(\lambda_0^{(2)}\right)^3\tanh\lambda_0^{(2)}d_0\lambda_n^{(2)}\tan\lambda_n^{(2)}d_0 \\ c_{n0}^{(1)} &= -K\lambda_0^{(2)}\tanh\lambda_0^{(2)}d_0\left(\lambda_n^{(2)}\right)^3\tan\lambda_n^{(2)}d_0 \\ c_{nn}^{(1)} &= K\left(\left(\lambda_n^{(2)}\right)^3\tan\lambda_n^{(2)}d_0\right)\times\left(\lambda_n^{(2)}\tan\lambda_n^{(2)}d_0\right) \end{aligned} \tag{E9}$$

$$
\begin{aligned}
c_{00}^{(2)} &= -K\left(\lambda_0^{(2)}\right)^4 \tanh^2 \lambda_0^{(2)} d_0 \\
c_{0n}^{(2)} &= K\left(\lambda_0^{(2)}\right)^3 \tanh \lambda_0^{(2)} d_0 \lambda_n^{(2)} \tan \lambda_n^{(2)} d_0 \\
c_{n0}^{(2)} &= -K\lambda_0^{(2)} \tanh \lambda_0^{(2)} d_0 \left(\lambda_n^{(2)}\right)^3 \tan \lambda_n^{(2)} d_0 \\
c_{nn}^{(2)} &= K\left(\left(\lambda_n^{(2)}\right)^3 \tan \lambda_n^{(2)} d_0\right) \times \left(\lambda_n^{(2)} \tan \lambda_n^{(2)} d_0\right)
\end{aligned}
\tag{E10}
$$

$$
\begin{aligned}
c_{00}^{(3)} &= -K\left(\lambda_0^{(4)}\right)^4 \tanh^2 \lambda_0^{(4)} d_0 \\
c_{0n}^{(3)} &= K\left(\lambda_0^{(4)}\right)^3 \tanh \lambda_0^{(4)} d_0 \lambda_n^{(4)} \tan \lambda_n^{(4)} d_0 \\
c_{n0}^{(3)} &= -K\lambda_0^{(4)} \tanh \lambda_0^{(4)} d_0 \left(\lambda_n^{(4)}\right)^3 \tan \lambda_n^{(4)} d_0 \\
c_{nn}^{(3)} &= K\left(\left(\lambda_n^{(4)}\right)^3 \tan \lambda_n^{(4)} d_0\right) \times \left(\lambda_n^{(4)} \tan \lambda_n^{(4)} d_0\right)
\end{aligned}
\tag{E11}
$$

$$
\begin{aligned}
c_{00}^{(4)} &= -K\left(\lambda_0^{(4)}\right)^4 \tanh^2 \lambda_0^{(4)} d_0 \\
c_{0n}^{(4)} &= K\left(\lambda_0^{(4)}\right)^3 \tanh \lambda_0^{(4)} d_0 \lambda_n^{(4)} \tan \lambda_n^{(4)} d_0 \\
c_{n0}^{(4)} &= -K\lambda_0^{(4)} \tanh \lambda_0^{(4)} d_0 \left(\lambda_n^{(4)}\right)^3 \tan \lambda_n^{(4)} d_0 \\
c_{nn}^{(4)} &= K\left(\left(\lambda_n^{(4)}\right)^3 \tan \lambda_n^{(4)} d_0\right) \times \left(\lambda_n^{(4)} \tan \lambda_n^{(4)} d_0\right)
\end{aligned}
\tag{E12}
$$

$$
\begin{aligned}
d_{00}^{(1)} &= e^{\mathrm{i}\lambda_0^{(2)} b_1} c_{00}^{(1)} \\
d_{0n}^{(1)} &= e^{-\lambda_n^{(2)} b_1} c_{0n}^{(1)} \\
d_{n0}^{(1)} &= e^{\mathrm{i}\lambda_0^{(2)} b_1} c_{n0}^{(1)} \\
d_{nn}^{(1)} &= e^{-\lambda_n^{(2)} b_1} c_{nn}^{(1)}
\end{aligned}
\tag{E13}
$$

$$
\begin{aligned}
d_{00}^{(2)} &= e^{\mathrm{i}\lambda_0^{(2)} b_1} c_{00}^{(2)} \\
d_{0n}^{(2)} &= e^{-\lambda_n^{(2)} b_1} c_{0n}^{(2)} \\
d_{n0}^{(2)} &= e^{\mathrm{i}\lambda_0^{(2)} b_1} c_{n0}^{(2)} \\
d_{nn}^{(2)} &= e^{-\lambda_n^{(2)} b_1} c_{nn}^{(2)}
\end{aligned}
\tag{E14}
$$

$$
\begin{aligned}
D_{00}^{(3)} &= e^{\mathrm{i}\lambda_0^{(4)} b_2} c_{00}^{(3)} \\
D_{0n}^{(3)} &= e^{-\lambda_n^{(4)} b_2} c_{0n}^{(3)} \\
D_{n0}^{(3)} &= e^{\mathrm{i}\lambda_0^{(4)} b_2} c_{n0}^{(3)} \\
D_{nn}^{(3)} &= e^{-\lambda_n^{(4)} b_2} c_{nn}^{(3)}
\end{aligned}
\tag{E15}
$$

$$\begin{aligned} D_{00}^{(4)} &= e^{\mathrm{i}\lambda_0^{(4)} b_2} c_{00}^{(4)} \\ D_{0n}^{(4)} &= e^{-\lambda_n^{(4)} b_2} c_{0n}^{(4)} \\ D_{n0}^{(4)} &= e^{\mathrm{i}\lambda_0^{(4)} b_2} c_{n0}^{(4)} \\ D_{nn}^{(4)} &= e^{-\lambda_n^{(4)} b_2} c_{nn}^{(4)} \end{aligned} \tag{E16}$$

$$f_n^{(1)} = \int_{-d_0}^{0} Z_o^{(1)}(z) Y_n^{(2)}(z)\, dz, n = 0, 1, 2, \cdots, N \tag{E17}$$

$$p_{nm}^{(1)} = \int_{-d_0}^{0} Z_m^{(1)}(z) Y_n^{(2)}(z)\, dz,\ n = 0, 1, 2, \cdots, N; m = 0, 1, 2, \cdots, M \tag{E18}$$

$$p_{nm}^{(2)} = \int_{-d_0}^{0} Z_m^{(3)}(z) Y_n^{(2)}(z)\, dz,\ n = 0, 1, 2, \cdots, N; m = 0, 1, 2, \cdots, M \tag{E19}$$

$$p_{nm}^{(3)} = \int_{-d_0}^{0} Z_m^{(3)}(z) Y_n^{(4)}(z)\, dz,\ n = 0, 1, 2, \cdots, N; m = 0, 1, 2, \cdots, M \tag{E20}$$

$$p_{nm}^{(4)} = \int_{-d_0}^{0} Z_m^{(5)}(z) Y_n^{(4)}(z)\, dz,\ n = 0, 1, 2, \cdots, N; m = 0, 1, 2, \cdots, M \tag{E21}$$

$$\begin{aligned} q_{00}^{(1)} &= -\frac{\lambda_0^{(2)}}{k_0^{(1)} N_0^{(1)}} \int_{-d_0}^{0} Z_0^{(1)}(z) Y_0^{(2)}(z)\, dz \\ q_{0n}^{(1)} &= -\frac{\mathrm{i}\lambda_n^{(2)}}{k_0^{(1)} N_0^{(1)}} \int_{-d_0}^{0} Z_0^{(1)}(z) Y_0^{(2)}(z)\, dz \\ q_{m0}^{(1)} &= \frac{\mathrm{i}\lambda_0^{(2)}}{k_m^{(1)} N_m^{(1)}} \int_{-d_0}^{0} Z_0^{(1)}(z) Y_0^{(2)}(z)\, dz \\ q_{mn}^{(1)} &= -\frac{\lambda_n^{(2)}}{k_m^{(1)} N_m^{(1)}} \int_{-d_0}^{0} Z_0^{(1)}(z) Y_0^{(2)}(z)\, dz \end{aligned} \tag{E22}$$

$$\begin{aligned} q_{00}^{(2)} &= -\frac{\lambda_0^{(2)}}{k_0^{(3)} N_0^{(2)}} \int_{-d_0}^{0} Z_0^{(3)}(z) Y_0^{(2)}(z)\, dz \\ q_{0n}^{(2)} &= -\frac{\mathrm{i}\lambda_n^{(2)}}{k_0^{(3)} N_0^{(2)}} \int_{-d_0}^{0} Z_0^{(3)}(z) Y_0^{(2)}(z)\, dz \\ q_{m0}^{(2)} &= \frac{\mathrm{i}\lambda_0^{(2)}}{k_m^{(3)} N_m^{(2)}} \int_{-d_0}^{0} Z_0^{(3)}(z) Y_0^{(2)}(z)\, dz \\ q_{mn}^{(2)} &= -\frac{\lambda_n^{(2)}}{k_m^{(3)} N_m^{(2)}} \int_{-d_0}^{0} Z_0^{(3)}(z) Y_0^{(2)}(z)\, dz \end{aligned} \tag{E23}$$

$$
\begin{aligned}
q_{00}^{(3)} &= -\frac{\lambda_0^{(4)}}{k_0^{(3)}N_0^{(3)}}\int_{-d_0}^{0} Z_0^{(3)}(z)Y_0^{(4)}(z)\,dz\\
q_{0n}^{(3)} &= -\frac{\mathrm{i}\lambda_n^{(4)}}{k_0^{(3)}N_0^{(3)}}\int_{-d_0}^{0} Z_0^{(3)}(z)Y_0^{(4)}(z)\,dz\\
q_{m0}^{(3)} &= \frac{\mathrm{i}\lambda_0^{(4)}}{k_m^{(3)}N_m^{(3)}}\int_{-d_0}^{0} Z_0^{(3)}(z)Y_0^{(4)}(z)\,dz\\
q_{mn}^{(3)} &= -\frac{\lambda_n^{(4)}}{k_m^{(3)}N_m^{(3)}}\int_{-d_0}^{0} Z_0^{(3)}(z)Y_0^{(4)}(z)\,dz
\end{aligned}
\tag{E24}
$$

$$
\begin{aligned}
q_{00}^{(4)} &= -\frac{\lambda_0^{(4)}}{k_0^{(5)}N_0^{(4)}}\int_{-d_0}^{0} Z_0^{(5)}(z)Y_0^{(4)}(z)\,dz\\
q_{0n}^{(4)} &= -\frac{\mathrm{i}\lambda_n^{(4)}}{k_0^{(5)}N_0^{(4)}}\int_{-d_0}^{0} Z_0^{(5)}(z)Y_0^{(4)}(z)\,dz\\
q_{m0}^{(4)} &= \frac{\mathrm{i}\lambda_0^{(4)}}{k_m^{(5)}N_m^{(4)}}\int_{-d_0}^{0} Z_0^{(5)}(z)Y_0^{(4)}(z)\,dz\\
q_{mn}^{(4)} &= -\frac{\lambda_n^{(4)}}{k_m^{(5)}N_m^{(4)}}\int_{-d_0}^{0} Z_0^{(5)}(z)Y_0^{(4)}(z)\,dz
\end{aligned}
\tag{E25}
$$

$$
\begin{aligned}
r_{00}^{(1)} &= -e^{\mathrm{i}\lambda_0^{(2)}b_1}q_{00}^{(1)}\\
r_{0n}^{(1)} &= -e^{-\lambda_n^{(2)}b_1}q_{0n}^{(1)}\\
r_{m0}^{(1)} &= -e^{\mathrm{i}\lambda_0^{(2)}b_1}q_{m0}^{(1)}\\
r_{mn}^{(1)} &= -e^{-\lambda_n^{(2)}b_1}q_{mn}^{(1)}
\end{aligned}
\tag{E26}
$$

$$
\begin{aligned}
r_{00}^{(2)} &= -e^{\mathrm{i}\lambda_0^{(2)}b_1}q_{00}^{(2)}\\
r_{0n}^{(2)} &= -e^{-\lambda_n^{(2)}b_1}q_{0n}^{(2)}\\
r_{m0}^{(2)} &= -e^{\mathrm{i}\lambda_0^{(2)}b_1}q_{m0}^{(2)}\\
r_{mn}^{(2)} &= -e^{-\lambda_n^{(2)}b_1}q_{mn}^{(2)}
\end{aligned}
\tag{E27}
$$

$$
\begin{aligned}
R_{00}^{(3)} &= -e^{\mathrm{i}\lambda_0^{(4)}b_2}q_{00}^{(3)}\\
R_{0n}^{(3)} &= -e^{-\lambda_n^{(4)}b_2}q_{0n}^{(3)}\\
R_{m0}^{(3)} &= -e^{\mathrm{i}\lambda_0^{(4)}b_2}q_{m0}^{(3)}\\
R_{mn}^{(3)} &= -e^{-\lambda_n^{(4)}b_2}q_{mn}^{(3)}
\end{aligned}
\tag{E28}
$$

$$
\begin{aligned}
R_{00}^{(4)} &= -e^{\mathrm{i}\lambda_0^{(4)}b_2}q_{00}^{(4)}\\
R_{0n}^{(4)} &= -e^{-\lambda_n^{(4)}b_2}q_{0n}^{(4)}\\
R_{m0}^{(4)} &= -e^{\mathrm{i}\lambda_0^{(4)}b_2}q_{m0}^{(4)}\\
R_{mn}^{(4)} &= -e^{-\lambda_n^{(4)}b_2}q_{mn}^{(4)}
\end{aligned}
\tag{E29}
$$

$$N_0^{(1)} = \int_{-d_1}^{0} \left(Z_o^{(1)}(z)\right)^2 dz$$
$$N_m^{(1)} = \int_{-d_1}^{0} \left(Z_m^{(1)}(z)\right)^2 dz, m = 1,2,3,\cdots,M \tag{E30}$$

$$N_0^{(2)} = \int_{-d_0}^{0} \left(Z_o^{(3)}(z)\right)^2 dz$$
$$N_{(m}^{(2)} = \int_{-d_0}^{0} \left(Z_m^{(3)}(z)\right)^2 dz, m = 1,2,3,\cdots,M \tag{E31}$$

$$N_0^{(3)} = \int_{-d_0}^{0} \left(Z_o^{(3)}(z)\right)^2 dz$$
$$N_m^{(3)} = \int_{-d_0}^{0} \left(Z_m^{(3)}(z)\right)^2 dz, m = 1,2,3,\cdots,M \tag{E32}$$

$$N_0^{(4)} = \int_{-d_0}^{0} \left(Z_o^{(5)}(z)\right)^2 dz$$
$$N_m^{(4)} = \int_{-d_0}^{0} \left(Z_m^{(5)}(z)\right)^2 dz, m = 1,2,3,\cdots,M \tag{E33}$$

$$v_{00}^{(2)} = e^{ik_0^{(3)}D_s}$$
$$v_{mm}^{(2)} = e^{-k_m^{(3)}D_s} \tag{E34}$$

$$v_{00}^{(3)} = e^{ik_0^{(3)}D_s}$$
$$v_{mm}^{(3)} = e^{-k_m^{(3)}D_s} \tag{E35}$$

$$u_{00}^{(2)} = e^{ik_0^{(3)}D_s} \int_{-d_0}^{0} Y_0^{(2)}(z) Z_0^{(3)}(z)\, dz$$
$$u_{0m}^{(2)} = e^{-k_m^{(3)}D_s} \int_{-d_0}^{0} Y_0^{(2)}(z) Z_m^{(3)}(z)\, dz$$
$$u_{n0}^{(2)} = e^{-ik_0^{(3)}D_s} \int_{-d_0}^{0} Y_n^{(2)}(z) Z_0^{(3)}(z)\, dz$$
$$u_{nm}^{(2)} = e^{k_m^{(3)}D_s} \int_{-d_0}^{0} Y_n^{(2)}(z) Z_m^{(3)}(z)\, dz \tag{E36}$$

$$
\begin{aligned}
u_{00}^{(3)} &= e^{ik_0^{(3)}D_s} \int_{-d_0}^{0} Y_0^{(4)}(z) Z_0^{(3)}(z)\, dz \\
u_{0m}^{(3)} &= e^{-k_m^{(3)}D_s} \int_{-d_0}^{0} Y_0^{(4)}(z) Z_m^{(3)}(z)\, dz \\
u_{n0}^{(3)} &= e^{-ik_0^{(3)}D_s} \int_{-d_0}^{0} Y_n^{(4)}(z) Z_0^{(3)}(z)\, dz \\
u_{nm}^{(3)} &= e^{k_m^{(3)}D_s} \int_{-d_0}^{0} Y_n^{(4)}(z) Z_m^{(3)}(z)\, dz
\end{aligned}
\tag{E37}
$$

REFERENCES

[1]A. Sahu, N. Yadav, and K. Sudhakar, "Floating photovoltaic power plant: A review," Renew. Sustain. Energy Rev. **66**, 815 (2016).

[2]S. Z. Golroodbari and W. van Sark, "Simulation of performance differences between offshore and land-based photovoltaic systems," Prog. Photovolt.: Res. Appl. **28**, 873 (2020).

[3]Xinhua, "Mining subsidence areas in East China's Anhui turned into floating PV power station," https://english.news.cn/20220826/62dcd91bd23a440da34f1ebba9df27dd/c.html, 26/08/2022.

[4]A. Ghosh, "A comprehensive review of water based PV: Flotavoltaics, under water, offshore and canal top," Ocean Eng. **281**, 115044 (2023).

[5]Y.-K. Choi and J.-H. Lee, "Structural safety assessment of ocean-floating photovoltaic structure model," Israel J. Chem. **55**, 1081–1090 (2015).

[6]J. Dai, C. Zhang, H. V. Lim, K. K. Ang, X. Qian, J. L. H. Wong, S. T. Tan, and C. L. Wang, "Design and construction of floating modular photovoltaic system for water reservoirs," Energy **191**, 116549 (2020).

[7]A. Al-Yacouby, E. R. B. A. Halim, and M. Liew, "Hydrodynamic analysis of floating offshore solar farms subjected to regular waves," in *Advances in Manufacturing Engineering: Selected articles from ICMMPE 2019* (Springer, 2020) pp. 375–390.

[8]P. Xu and P. R. Wellens, "Theoretical analysis of nonlinear fluid–structure interaction between large-scale polymer offshore floating photovoltaics and waves," Ocean Eng. **249**, 110829 (2022).

[9]D. Zhang, J. Du, Z. Yuan, S. Yu, and H. Li, "Motion characteristics of large arrays of modularized floating bodies with hinge connections," Phys. Fluids **35**, 077107 (2023).

[10]C. Michailides, E. Loukogeorgaki, and D. C. Angelides, "Response analysis and optimum configuration of a modular floating structure with flexible connectors," Appl. Ocean Res. **43**, 112 (2013).

[11]G.-H. Lee, J.-W. Choi, J.-H. Seo, and H. Ha, "Comparative study of effect of wind and wave load on floating PV: Computational simulation and design method," J. Korean Soc. Manuf. Process Eng. **18**, 9 (2019).

[12]J.-H. Lee, K.-J. Paik, S.-H. Lee, J. Hwangbo, and T.-H. Ha, "Experimental and numerical study on the characteristics of motion and load for a floating solar power farm under regular waves," J. Mar. Sci. Eng. **10**, 565 (2022).

[13]K. Trapani, D. L. Millar, and H. C. Smith, "Novel offshore application of photovoltaics in comparison to conventional marine renewable energy technologies," Renew. Energy **50**, 879 (2013).

[14]C. Fox and V. A. Squire, "Reflection and transmission characteristics at the edge of shore fast sea ice," Journal of Geophysical Research: Oceans **95**, 11629–11639 (1990).

[15]M. Meylan and V. A. Squire, "Finite-floe wave reflection and transmission coefficients from a semi-infinite model," J. Geophys. Res.: Oceans **98**, 12537 (1993).

[16]A. I. Andrianov and A. J. Hermans, "The influence of water depth on the hydroelastic response of a very large floating platform," Mar. Struct. **16**, 355 (2003).

[17]M. Meylan and I. Sturova, "Time-dependent motion of a two-dimensional floating elastic plate," J. Fluids Struct. **25**, 445 (2009).

[18]P. Maiti and B. Mandal, "Water wave scattering by an elastic plate floating in an ocean with a porous bed," Appl. Ocean Res. **47**, 73 (2014).

[19]M. Singh, M. H. Meylan, and R. Gayen, "Time-domain motion of a floating or obliquely submerged non-uniform elastic plate," Phys. Fluids **35**, 047117 (2023).

[20]O. I. Gusev, G. S. Khakimzyanov, V. S. Skiba, and L. B. Chubarov, "Numerical modeling of the long surface wave impact on a partially immersed structure in a coastal zone: Solitary waves over a flat slope," Phys. Fluids **35**, 087124 (2023).

[21]C. D. Wang and M. H. Meylan, "The linear wave response of a floating thin plate on water of variable depth," Appl. Ocean Res. **24**, 163 (2002).

[22]Y. Guo, Y. Liu, and X. Meng, "Oblique wave scattering by a semi-infinite elastic plate with finite draft floating on a step topography," Acta Oceanologica Sinica **35**, 113 (2016).

[23]R. Porter and D. Evans, "Scattering of flexural waves by multiple narrow cracks in ice sheets floating on water," Wave Motion **43**, 425 (2006).

[24]Z. F. Li, G. X. Wu, and K. Ren, "Wave diffraction by multiple arbitrary shaped cracks in an infinitely extended ice sheet of finite water depth," J. Fluid Mech. **893**, A14 (2020).

[25]A. Marchenko, "Resonance interactions of waves in an ice channel," J. Appl. Math. Mech. **61**, 931 (1997).

[26]K. Ren, G. Wu, and G. Thomas, "Wave excited motion of a body floating on water confined between two semi-infinite ice sheets," Phys. Fluids **28**, 127101 (2016).

[27]Y. Shi, Z. Li, and G. Wu, "Interaction of wave with multiple wide polynyas," Phys. Fluids **31**, 067111 (2019).

[28]V. K. Kostikov, M. Hayatdavoodi, and R. C. Ertekin, "Drift of elastic floating ice sheets by waves and current: Multiple sheets," Phys. Fluids **34**, 057113 (2022).

[29]G. B. Arfken, H. J. Weber, and F. E. Harris, *Mathematical Methods for Physicists: A Comprehensive Guide 7th ed.* (Elsevier Pte Ltd, 2013).

[30]H. Lamb, *Hydrodynamics. 6th Edition* (Cambridge University Press, 1932).

[31]A. G. Greenhill, "Wave motion in hydrodynamics," Am. J. Math. **9**, 62–112 (1887).

[32]S. Zheng, M. H. Meylan, D. Greaves, and G. Iglesias, "Water-wave interaction with submerged porous elastic disks," Phys. Fluids **32**, 047106 (2020).

[33]Z. Li, Y. Shi, and G. Wu, "Interaction of ocean wave with a harbor covered by an ice sheet," Physics of Fluids **33**, 057109 (2021).

[34]B. Teng, L. Cheng, and L. S. X, "Modified eigenfunction expansion methods of water waves with a semi-infinite elastic plate," Appl. Ocean Res. **23**, 357 (2001).

[35]M. Meylan and V. A. Squire, "The response of ice floes to ocean waves," J. Geophys. Res.: Oceans **99**, 891 (1994).

[36]C. Zhang, Q. Zhuang, J. Li, L. Huang, and D. Ning, "Hydroelastic investigation on a pile breakwater integrated with a flexible tail for long-wave attenuation," China Ocean Eng. **36**, 667–681 (2022).

Resonance mechanism of hydroelastic response of multi-patch floating photovoltaic structure in water waves over stepped seabed

Zhang, Chongwei

2023-10-25

Zhang C, Wang P, Huang L, et al., (2023) Resonance mechanism of hydroelastic response of multi-patch floating photovoltaic structure in water waves over stepped seabed. Physics of Fluids, Volume 35, Issue 10, October 2023, Article number 107137

https://doi.org/10.1063/5.0169061